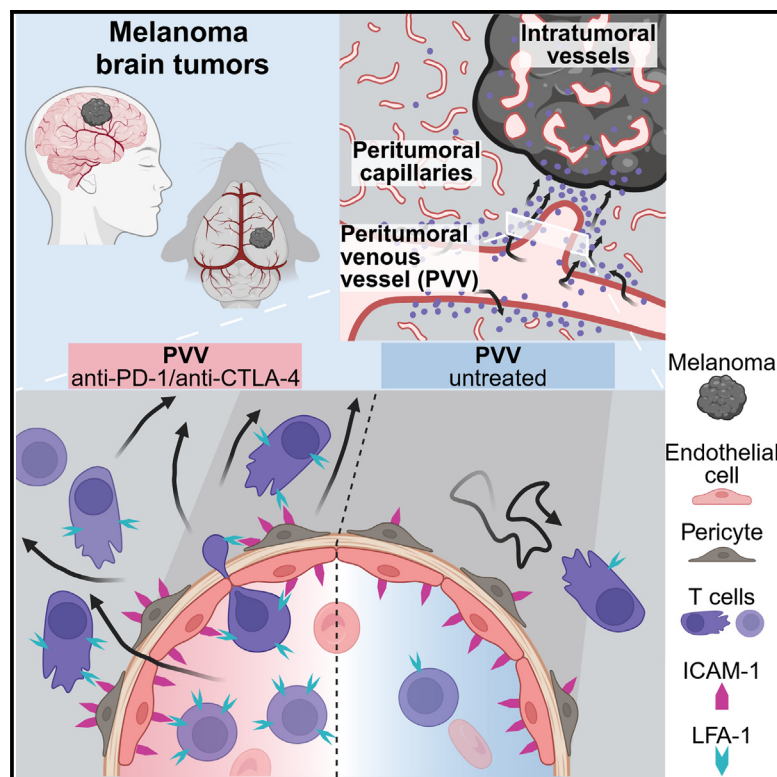


Immunity

T lymphocyte recruitment to melanoma brain tumors depends on distinct venous vessels

Graphical abstract



Authors

Julia M. Messmer, Calvin Thommek,
Manuel Piechutta, ..., Michael Hölzel,
Matthia A. Karreman, Frank Winkler

Correspondence

m.karreman@dkfz-heidelberg.de
(M.A.K.),
frank.winkler@
med.uni-heidelberg.de (F.W.)

In brief

How T cells are recruited to brain tumors from the blood remains unclear. Messmer et al. identify peritumoral venous vessels (PVVs) as key structures for T cell recruitment to melanoma brain tumors. PVVs are the sites of T cell extravasation and facilitate rapid T cell migration under immune checkpoint inhibition. T cell recruitment and antitumor immunity were dependent on ICAM-1.

Highlights

- PVVs are key structures for T cell recruitment to melanoma brain tumors
- Anti-PD-1/CTLA-4 inhibitors boost T cell recruitment through PVVs
- T cell recruitment and antitumor immunity is dependent on ICAM-1 expression on PVVs
- ICAM-1 on PVVs correlates with T cell infiltration in human melanoma brain metastases



Article

T lymphocyte recruitment to melanoma brain tumors depends on distinct venous vessels

Julia M. Messmer,^{1,2,3} Calvin Thommek,^{1,2} Manuel Piechutta,¹ Varun Venkataramani,^{4,5} Rebekka Wehner,^{6,7,8,15} Dana Westphal,^{7,9} Marc Schubert,⁴ Chanté D. Mayer,^{1,4} Maike Effern,³ Anna S. Berghoff,^{10,11} Daniel Hinze,³ Iris Helfrich,^{12,13,14} Dirk Schadendorf,¹⁴ Wolfgang Wick,^{1,4} Michael Hözel,³ Matthias A. Karreman,^{1,4,16,*} and Frank Winkler^{1,4,16,17,*}

¹Clinical Cooperation Unit Neurooncology, German Cancer Consortium (DKTK), German Cancer Research Center (DKFZ), 69120 Heidelberg, Germany

²Faculty of Biosciences, Heidelberg University, 69120 Heidelberg, Germany

³Institute of Experimental Oncology (IEO), Medical Faculty, University Hospital Bonn, University of Bonn, 53127 Bonn, Germany

⁴Neurology Clinic and National Center for Tumor Diseases, University Hospital Heidelberg, INF 400, 69120 Heidelberg, Germany

⁵Department of Functional Neuroanatomy, University Hospital Heidelberg, 69120 Heidelberg, Germany

⁶Faculty of Medicine Carl Gustav Carus, Institute of Immunology, TU Dresden, 01307 Dresden, Germany

⁷Partner Site Dresden, National Center for Tumor Diseases (NCT), 01307 Dresden, Germany

⁸German Cancer Consortium (DKTK), partner site Dresden, 01307 Dresden, Germany

⁹Department of Dermatology, Medical Faculty and University Hospital Carl Gustav Carus, TU Dresden, 01307 Dresden, Germany

¹⁰Department of Medicine I, Division of Oncology, Medical University of Vienna, Vienna, Austria

¹¹Comprehensive Cancer Center, Medical University of Vienna, Vienna, Austria

¹²Medical Faculty of the Ludwig Maximilian University of Munich, Department of Dermatology and Allergology, Frauenlobstrasse 9-11, 80377 Munich, Germany

¹³German Cancer Consortium (DKTK), Partner Site Munich, Munich, Germany

¹⁴Department of Dermatology, University Hospital Essen, Hufelandstraße 55, 45147 Essen, Germany

¹⁵German Cancer Research Center (DKFZ), Heidelberg, Germany

¹⁶These authors contributed equally

¹⁷Lead contact

*Correspondence: m.karreman@dkfz-heidelberg.de (M.A.K.), frank.winkler@med.uni-heidelberg.de (F.W.)

<https://doi.org/10.1016/j.immuni.2024.09.003>

SUMMARY

To improve immunotherapy for brain tumors, it is important to determine the principal intracranial site of T cell recruitment from the bloodstream and their intracranial route to brain tumors. Using intravital microscopy in mouse models of intracranial melanoma, we discovered that circulating T cells preferably adhered and extravasated at a distinct type of venous blood vessel in the tumor vicinity, peritumoral venous vessels (PVVs). Other vascular structures were excluded as alternative T cell routes to intracranial melanomas. Anti-PD-1/CTLA-4 immune checkpoint inhibitors increased intracranial T cell motility, facilitating migration from PVVs to the tumor and subsequently inhibiting intracranial tumor growth. The endothelial adhesion molecule ICAM-1 was particularly expressed on PVVs, and, in samples of human brain metastases, ICAM-1 positivity of PVV-like vessels correlated with intratumoral T cell infiltration. These findings uncover a distinct mechanism by which the immune system can access and control brain tumors and potentially influence other brain pathologies.

INTRODUCTION

Brain metastasis is a frequent complication of melanoma and is associated with a poor prognosis for patients, with a median survival of 4–6 months.^{1,2} The brain has long been considered an immune-privileged organ.³ However, recently a lymphatic system of the meninges composed of lymphatic vessels located in close proximity along the superior sagittal sinus, which allows immune surveillance of brain-derived antigens, was discovered both in mice^{4,5} and in humans.^{6,7} Clinical trials of melanoma

brain metastases patients showed that treatment with immune checkpoint inhibition (ICI) leads to intracranial responses in up to 50%–65% of patients.^{8,9} Although these preclinical and clinical observations highlight the potential of immunotherapeutic approaches for the treatment of intracranial melanoma, the exact anatomical and molecular mechanisms of immune cell recruitment to intracranial tumor lesions are currently still not identified. To improve immunotherapy for brain tumors, it is important to address critical unresolved questions in brain tumor immunology: what is the principal intracranial site of T cell



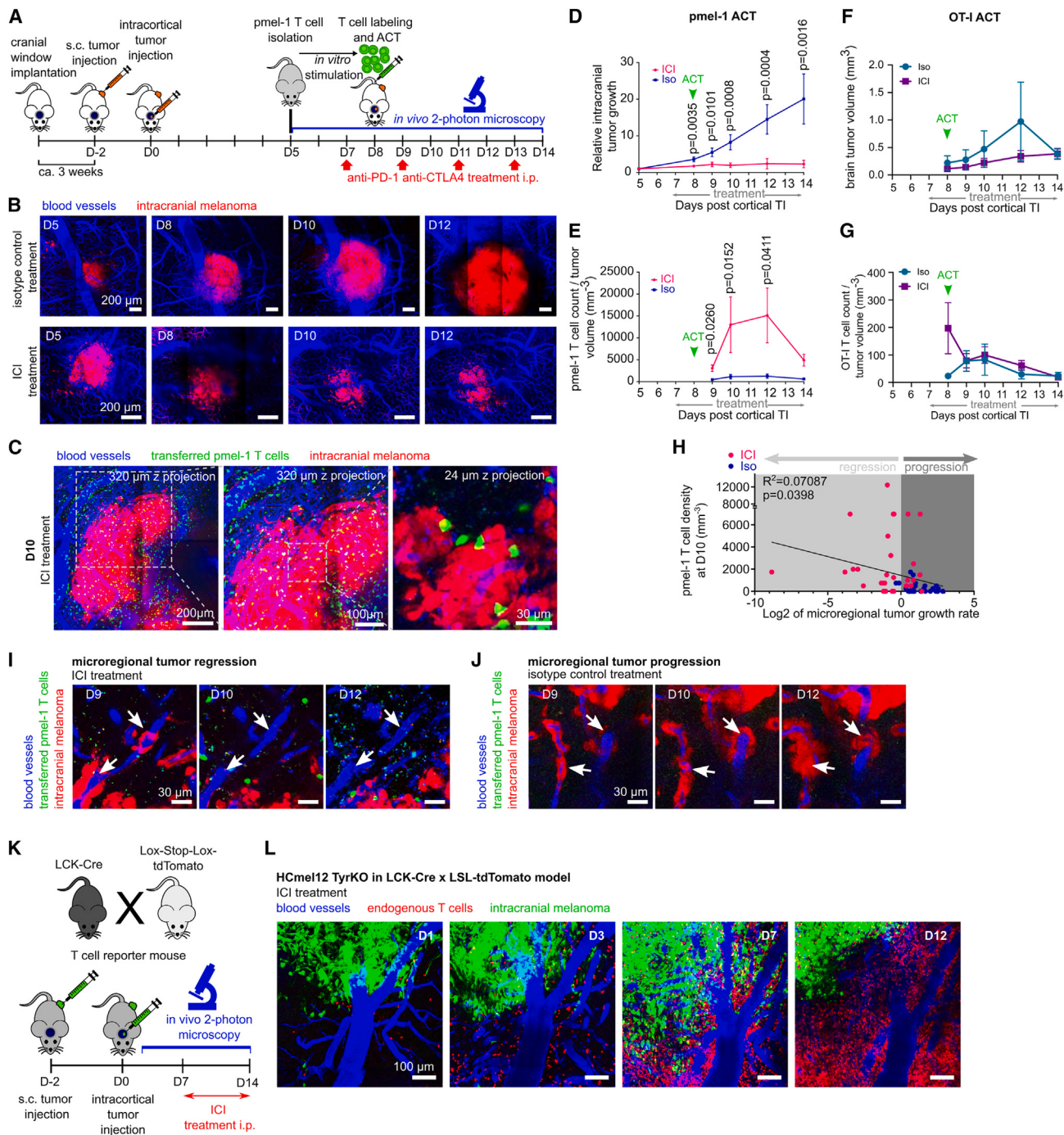


Figure 1. Dynamic infiltration of T cells can control brain tumor growth

(A) Schematic experimental design for IVM of an adoptive CD8⁺ T cell transfer (ACT) model for intracranial melanoma.

(B and C) IVM of intracranial tumor growth of ICI or isotype-control-treated HCmel12 TyrKO melanoma over time shown as maximum intensity projection (MIP) (B) and of intracranial CD8⁺ pmel-1 T cell infiltration under ICI treatment at day 10 post cortical TI (C) MIPs of 320, 320, and 24 μm depth from left to right.

(D and E) Quantification of intracranial tumor growth normalized to the tumor volume on day 5 post TI (D) and peri- and intratumoral T cell count normalized to tumor volume (E) of HCmel12 TyrKO intracranial melanoma under ACT with ICI or isotype control. $n = 6$ mice per group on days 5–12; day 14 $n = 6$ mice ICI, $n = 5$ mice Iso, two-tailed ratio paired t test per time point (D), and Mann-Whitney test (E).

(F and G) Quantification of brain tumor volume (F) and peri- and intratumoral T cell count normalized to tumor volume (G) of HCmel12 TyrKO intracranial melanoma under ACT with antigen-unspecific OT-I T cells on day 8 with ICI or isotype control treatment starting on day 7 post cortical TI. $n = 4$ mice ICI treated; $n = 3$ isotype-control-treated mice.

(legend continued on next page)

recruitment from the blood stream and what “route” do T cells use to access brain tumors? Can multiparameter imaging be used to better understand how anti-programmed cell death protein 1 (PD-1)/cytotoxic T lymphocyte antigen-4 (CTLA-4) immune checkpoint inhibitors enhance immunological control of brain tumors, as recently demonstrated in another approach for prediction of overall efficacy of PD-1 blockade?¹⁰

To unravel these basic cellular mechanisms, we established mouse models of intracranial melanoma using intravital two-photon microscopy (IVM). By visualizing spatiotemporal dynamics of T cell recruitment to brain tumors, we uncovered sites of intraluminal T cell attachment and extravasation in distinct, intercellular adhesion molecule 1 (ICAM-1)-expressing peritumoral venous vessels (PVVs), and the PVV perivascular space as a site of increased T cell abundance and T cell motility, contributing to efficient tumor homing and intracranial tumor growth suppression.

RESULTS

Model allows real-time tracking of the interplay of brain tumor growth and infiltrating T cells

To study T cell dynamics and brain tumor growth in intracranial melanoma *in vivo*, we established an adoptive T cell transfer (ACT) model with two glycoprotein100 (gp100)-antigen-expressing syngeneic melanoma cell lines (Figure S1A). To mimic the situation in patients, a subcutaneous (s.c.) extracranial tumor was implanted followed by an intracranial tumor injection (TI) into the mouse brain cortex (Figure 1A), which enables more efficient T cell homing to brain tumors.^{11,12} Adoptively transferred fluorescent premelanosome protein (pmel)-1 CD8⁺ T cells (Figures S1B and S1C), specifically targeting gp100, were visualized by performing IVM in mice treated with anti-PD-1 and anti-CTLA-4 ICI or isotype (Iso) control antibodies (Figure 1A). Brain tumor growth (Figure 1B) and T cell infiltration in relation to the brain and tumor microenvironment (Figures 1C and S1D) could be readily detected at subcellular resolution and followed over time. This methodology allowed dynamic insights into the intracranial anti-tumor effects of ICI treatment (Figures 1B, 1D, and S1E). ICI increased the number of brain-homing, antigen-specific, pmel-1-transferred T cells as early as 1 day after ACT, which became pronounced in the subsequent 3 days in both models (Figures 1E and S1F). The growth of extracranial tumors was also reduced (Figures S1G and S1H). In contrast, adoptive transfer of tumor-antigen-unspecific OT-I T cells did not lead to a significant effect of ICI treatment compared with Iso control on brain tumor growth (Figure 1F) and resulted in a much lower OT-I T cell infiltration in the brain tumor microenvironment (Figure 1G).

Microregional presence of tumor-specific pmel-1 T cells was associated with a reduction in tumor growth or even tumor regression over time (Figures 1H–1J), supporting the concept

that the transferred pmel-1 T cells exert antitumor effects in the brain and indicating a selective entry of antigen-specific T cells into the brain parenchyma as key mechanism of antitumor immunity.

To study brain-homing and dynamic T cell-tumor-cell interactions of endogenous T cells, we next generated a transgenic T cell reporter mouse line. Lymphocyte protein tyrosine kinase (LCK)-Cre × Lox-Stop-Lox (LSL)-tdTomato mice express floxed tdTomato and Cre recombinase under a lymphocyte LCK promoter (Figure 1K), resulting in tdTomato expression in 92.4%–99.1% of CD4⁺ and CD8⁺ T cells isolated from lymph nodes and spleen (Figures S2A–S2C) but only in 0.5%–2.8% of non-T cell leukocytes (Figure S2D). Spectral flow cytometry of the immune composition of the brain tumors revealed similar specificity of tdTomato expression within the brain tumor microenvironment, with the vast majority of tdTomato⁺ CD45⁺ leukocytes being T cells, while only 2.83%–4.27% were NK1.1 positive and thus belonged to natural killer (NK) or NK T cells (NKT); contributions of other immune cell types, such as granulocytes, macrophages, B cells, dendritic cells (DCs), or microglia, remained negligible (Figures S2E and S2F).

Repetitive imaging of the whole tumor, peritumoral-, and non-affected brain areas enabled the tracking of T cell infiltration and dynamics at high resolution over 2 weeks *in vivo* (Figures 1K, 1L, S3A, and S3B). The tumor growth of both extracranial (Figure S3C) and intracranial (Figure S3D) melanomas in these LCK-Cre × LSL-tdTomato mice was inhibited under ICI treatment as compared with Iso control treatment, demonstrating that ICI treatment effectively inhibited intracranial tumor growth even without additional ACT administration. In summary, intravital imaging of these mouse models allowed dynamic insights into T cell-tumor interactions of both adoptively transferred and endogenous T cells and demonstrated the antitumor effects of ICI treatment in the murine brain.

T cells accumulate in the perivascular space of distinct PVVs

Four-dimensional imaging of T cell recruitment in both models revealed a particularly high density of T cells at a distinct anatomical site that was identified as large PVVs (Figures 2A and 2B), with a mean diameter of $78.3 \pm 12.48 \mu\text{m}$ and blood flow velocities of $13.8 \pm 1.3 \text{ mm/s}$ (Figures S3E–S3G), compatible with their venous nature,¹³ which drained into larger venous vessels and finally into the sagittal venous sinus. PVVs were detectable as early as 1 day following tumor implantation (Figure 2B), indicating that these are pre-existing blood vessels of the brain. Far less T cells were observed in brains of non-tumor-bearing mice receiving no therapy (Figures S3H–S3L). In healthy brains, accumulation of endogenous T cells around venous vessels anatomically similar to PVVs could also be observed (Figures S3H and S3I), suggesting that T cells already accumulate around

(H) Negative correlation by linear regression of microregional tumor growth rate ($\log 2$ of day 12 post TI regional tumor volume/day 9 regional tumor volume) with T cell density on day 10 post TI in HCmel12 TyrKO intracranial melanoma under ICI and Iso control treatment.

(I and J) IVM images of microregional tumor regression and pmel-1 T cell abundance under ICI treatment (I) and progression under control treatment (J) of HCmel12 TyrKO intracranial melanoma over time (MIPs of $20 \mu\text{m}$ depth).

(K and L) Schematic experimental design (K) for IVM of endogenous T cells of LCK-Cre × LSL-tdTomato reporter mice, and IVM images (L) of HCmel12 TyrKO intracranial melanoma growth in ICI-treated mice over time (MIPs of $30 \mu\text{m}$ depth). Intravenously injected tetramethylrhodamine-isothiocyanate (TRITC)-dextran (shown in blue) reveals the vessel lumen in (B), (C), (I), (J), and (L). See also Figures S1, S2, and S3A–S3D.

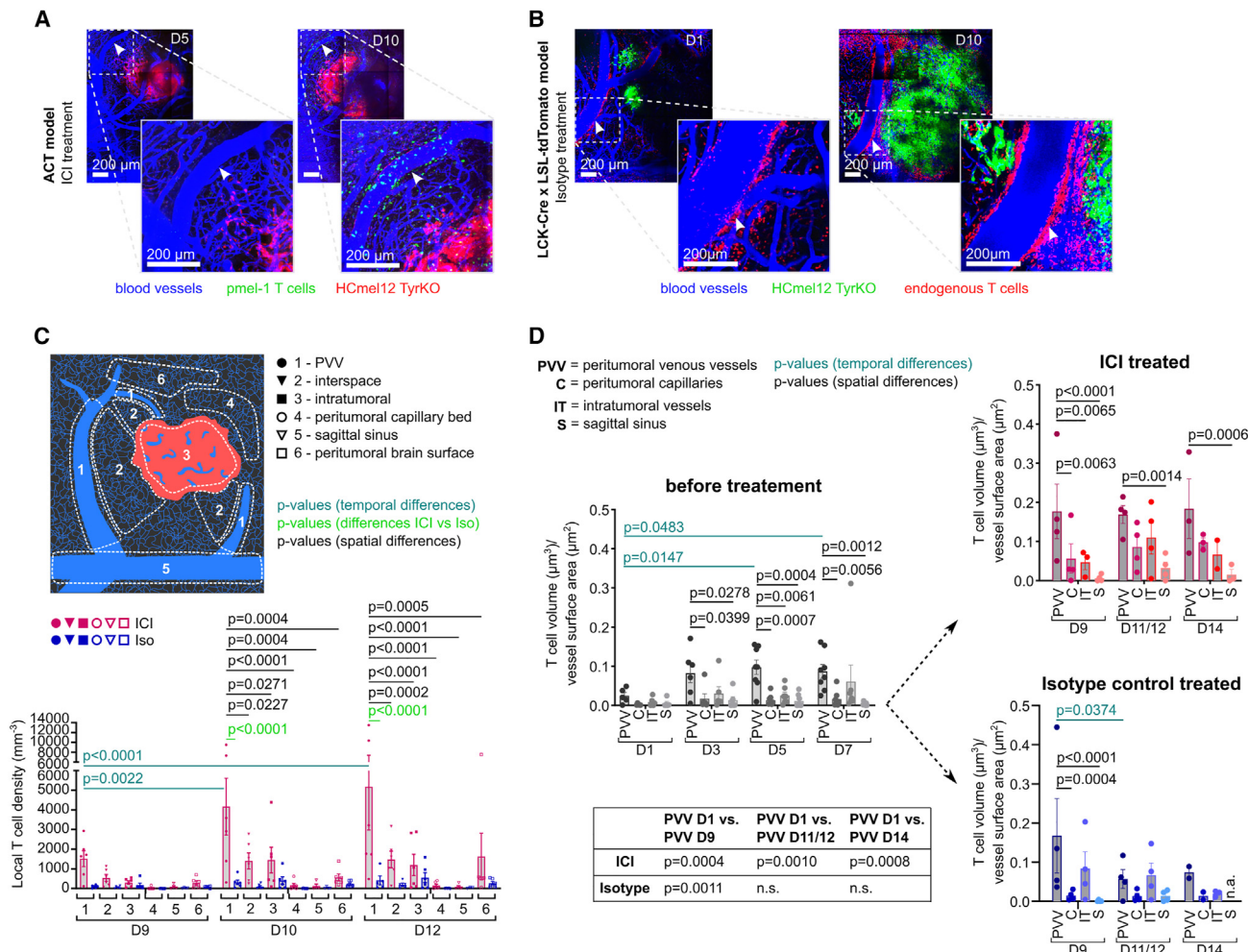


Figure 2. PVVs are the site of T cell homing to brain tumors

(A and B) IVM images of HCmel12 TyrKO ACT model of intracranial melanoma at days 5 and 10 post TI treated with ICI (A) and in LCK-Cre × LSL-TdTomato mice treated with isotype control at days 1 and 10 (B). Arrowheads indicate PVVs with high T cell density. Images are shown as MIPs of 230 μm depth on day 5, and 160 μm depth on day 10 for whole tumor overview and zooms (A), and as MIPs of 110 μm depth on day 1, and 40 μm depth on day 10 for whole tumor overview and zooms (B).

(C) Quantification of local T cell density of transferred pmel-1 T cells at days 9, 10, and 12 post TI at distinct peripheral regions and within intracranial HCmel12 TyrKO melanoma under ICI (red) or isotype control (blue) treatment. Analyzed regions are schematically depicted on the left, numbers 1–6 indicate different regions. $n = 6$ mice per group days 9 and 10, $n = 5$ mice per group day 12, two-way ANOVA with Tukey's post hoc test.

(D) Quantification of local T cell density of endogenous T cells in HCmel12 TyrKO intracranial melanoma in the LCK-Cre × LSL-TdTomato model before treatment onset (days 1–7, left part) treated with ICI (days 9–14, top right), or isotype control (days 9–14, bottom right) within 15 μm proximity of distinct vessel types (PVV, peritumoral capillaries, intratumoral vessels, and sagittal sinus). For statistical analysis using two-way ANOVA with Tukey's post hoc test all mice were pooled before treatment start (days 1–7) with $n = 8$ mice, upon treatment onset on day 7 after imaging the mice were split into two treatment groups with $n = 4$ mice per group. p values of temporal differences are shown in blue, p values of spatial differences are shown in black, p values of temporal differences at PVVs comparing day 1 before treatment with days 9, 11/12, and 14 ICI treated, or isotype control treated, are listed in the table of (D). Intravenously injected TRITC-dextran (blue) reveals the vessel lumen in (A) and (B). See also Figures S3E–S3L and S4.

these vessels in absence of a brain tumor and increasingly so when a tumor is present. In accordance with previous findings,¹⁴ we observed an increased T cell density in the brains of non-tumor-bearing mice around the sagittal venous sinus and at the brain surface, while only very few T cells were found in the cortical capillary bed (Figures S3H–S3L). Cortical sham injection of PBS did not increase T cell infiltration to the brain significantly compared with the already very low baseline T cell infiltration before injection (Figures S4A–S4C), indicating that local inflammation induced by the procedure of the injection alone, or the

prior surgical procedure, was minimal and did not relevantly affect T cell infiltration to the brain.

To elucidate local T cell dynamics and the exact route of T cells to intracranial tumors, we determined the number of pmel-1 T cells in different peritumoral and intratumoral regions at different time points following ACT under ICI treatment and Iso control (Figure 2C). Starting 2 days post ACT, T cell density at PVVs was significantly increased compared with the interspace region between PVV and tumor, intratumoral, peritumoral capillary bed, the sagittal venous sinus, and the peritumoral brain surface under

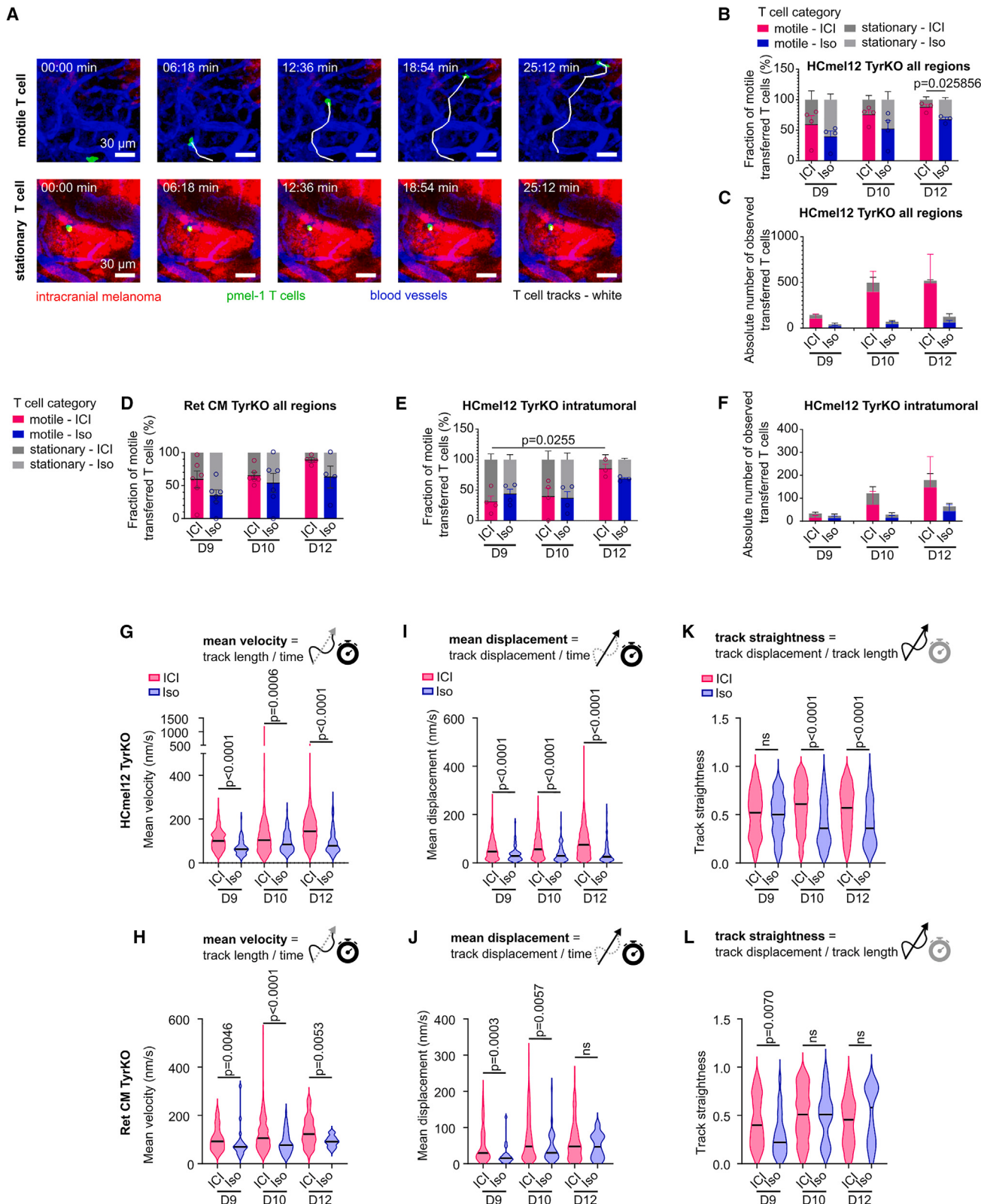


Figure 3. Motility and ICI-dependent activation patterns of brain-tumor-directed T cells

(A) Images of a time series analysis of one pmel-1 T cell categorized as “motile” (top row) and a pmel-1 T cell categorized as “stationary” (bottom row) over a time period of >25 min. MIPs of three-dimensional (3D) images, T cell tracks are shown in white. Motility parameters of transferred T cells in intracranial HCmel12

(legend continued on next page)

ICI treatment. With time, the T cell density at PVVs increased even more, the interregional spatiotemporal dynamics suggesting a PVV-induced T cell recruitment to the tumor region (Figure 2C). This was not seen in Iso-treated control mice (Figure 2C). Semi-automated analysis of infiltration dynamics of the more frequently detectable endogenous T cells in the LCK-Cre × LSL-tdTomato model confirmed a significant increase in T cell infiltration at PVVs in comparison with the capillary bed as early as days 3, 5, and 7 (Figure 2D, before treatment). Under ICI treatment, T cells in the vicinity of PVVs further increased and remained continuously higher than those in other regions over time (Figure 2D, upper right), whereas under Iso control treatment, T cell infiltration at PVVs decreased over time and was not significantly increased anymore at later time points (Figure 2D, lower right). In summary, early T cell accumulation at PVVs suggests a distinct role of these venous vessels for T cell recruitment to melanoma brain tumors, particularly under ICI treatment.

ICI treatment increases distinct parameters of T cell motility

An important aspect of lymphocyte homing and effector functionality is motility, with stationary or motile phenotypes that are linked to different functions,¹⁵ which has not been studied in the context of brain tumors yet. In general, T cell motility patterns have rarely been studied in the context of other cancers.^{16–18} ICI treatment moderately increased the overall fraction of motile transferred antigen-specific pmel-1 T cells *in vivo*, in both models of intracranial melanoma (Figures 3A–3D).

Limiting the analysis to intratumoral T cells, those displayed a higher fraction of stationary T cells on day 9 compared with day 12 (Figures 3E and 3F), indicating intratumoral antigen recognition on target cells early after ACT.^{16,17} By analyzing the overall dynamics of only those motile T cells that are en route to the tumor, we found that the T cell mean velocity and mean displacement were significantly higher in ICI vs. control groups for both melanoma models (Figures 3G–3J). T cell track straightness, an indicator for directed T cell movement, was significantly increased under ICI treatment at distinct time points in both tumor models (Figures 3K and 3L). Together, this suggests an increased potential for T cells to reach their target under ICI treatment, either by direct effects on T cells or indirect effects on the microenvironment.

T cells extravasate from PVVs and migrate particularly quickly in their perivascular space

Intravascular T cell rolling or crawling, necessary for T cell extravasation to the brain,^{19,20} almost exclusively occurred at PVVs

(Figures 4A and 4B), whereas at peritumoral capillaries, sites of perivascular tumor growth or intratumoral vessels (Figures 4B and 4C), fast-moving intraluminal T cells could mostly be observed without showing signs of stable attachment to the vascular wall. *Bona fide* T cell extravasation events were exclusively observed at PVVs, most prominently 1 day post ACT (Figures 4A and 4B; Videos S1, S2, S3, and S4). By comparing T cell motility of pmel-1 T cells at different brain and tumor regions (Figures 4D–4G), a spatial effect on T cell motility could be detected. T cells at PVVs and at PVV-associated peritumoral regions displayed the highest motility, which decreased with increasing proximity to the tumor, such as at the tumor edge, and exhibited lowest values intratumorally (Figures 4E–4G; Video S5). T cells at the tumor edge had a significantly higher track straightness under ICI compared with the Iso control (Figure 4G), suggesting that ICI facilitates T cell homing to tumor target cells.

Taken together, our data collectively indicate that PVVs provide structures that allow T cell migration at a fast pace once extravasated from the blood vessels. All in all, PVVs provide the basis for ICI-mediated efficient recruitment of high numbers of T cells to brain tumors and their subsequent antitumor effects.

PVVs with high T cell density are characterized by high vascular ICAM-1 expression

Next, we sought to investigate the molecular mechanism of T cell extravasation at PVVs, considering potential known molecules of lymphocyte-vascular interactions.^{21,22} ICAM-1 expression was evident for endothelial and adjacent abluminal cells in PVVs of cortically growing melanoma tumors (Figure S5A) but not clearly associated with any other blood vessel type or region in the brain or brain tumor (Figures S5A and S5B). Further analysis revealed that ICAM-1 expression colocalized partially with CD13 pericyte staining at PVVs of cortical tumors (Figures S6A–S6C). When a melanoma tumor grew in the striatum after local injection there, T cells infiltrated the tumor effectively (Figures S6D and S6E), similar to the situation found in cortical tumors. Again, T cells clustered particularly on large ICAM-1-positive vessels in the peritumoral region of the striatal tumors (Figures S6F–S6H). This indicated that (1) PVV structures are not limited to the cortex and its pre-existent large venous vessels and (2) ICAM-1 might be relevant for their function.

To further assess the immune cell composition of those tumors and to molecularly characterize vascular endothelial cells and pericytes in respect of their expression of the adhesion molecules ICAM-1 and vascular cell adhesion molecule 1 (VCAM-1), and to assess the expression of PD-1 and the ICAM-1 ligand lymphocyte function-associated antigen-1 (LFA-1) on T cells, we used

TyrKO melanoma, measured by IVM real-time time series analysis and T cell tracking. Angiogram was obtained through intravenous TRITC-dextran (shown in blue).

(B–F) Quantification of the fraction (B, D, and E) and absolute numbers (C and F) of motile and stationary pmel-1 T cells of all intratumoral and peritumoral regions combined (B–D) and intratumoral exclusively (E and F) of mice with HCmel12 TyrKO (B, C, E, and F) or Ret CM TyrKO (D) brain tumors treated with ICI or isotype control. For HCmel12 tumors *p* values were calculated using two-tailed, unpaired t test (B) and two-way ANOVA with Tukey's post hoc test (E) of data from days 9 and 10 *n* = 4 mice, day 12 *n* = 3 mice (B, C, E, and F). For Ret CM TyrKO tumors (D) data are from days 9 and 10 *n* = 6 mice, day 12 *n* = 4 mice per group. (G–L) Violin plots of the pmel-1 T cell motility parameters mean velocity (track length/time) (G and H), mean displacement (track displacement/time) (I and J) and track straightness (track displacement/track length) (K and L) of motile transferred pmel-1 T cells from all intratumoral and peritumoral regions combined on days 9, 10, and 12 post TI under ICI and isotype treatment in HCmel12 intracranial melanoma (G, I, and K) or in Ret CM TyrKO intracranial melanoma (H, J, and L). Mann-Whitney tests were performed per time point; for HCmel12 tumors (G, I, and K) *n* = 4 mice per group on days 9 and 10, *n* = 3 mice per group on day 12; for Ret CM TyrKO tumors (H, J, and L) T cell tracks of *n* = 6 mice per group on days 9 and 10, T cell tracks of *n* = 4 mice per group on day 12 were analyzed. Black bars represent medians.

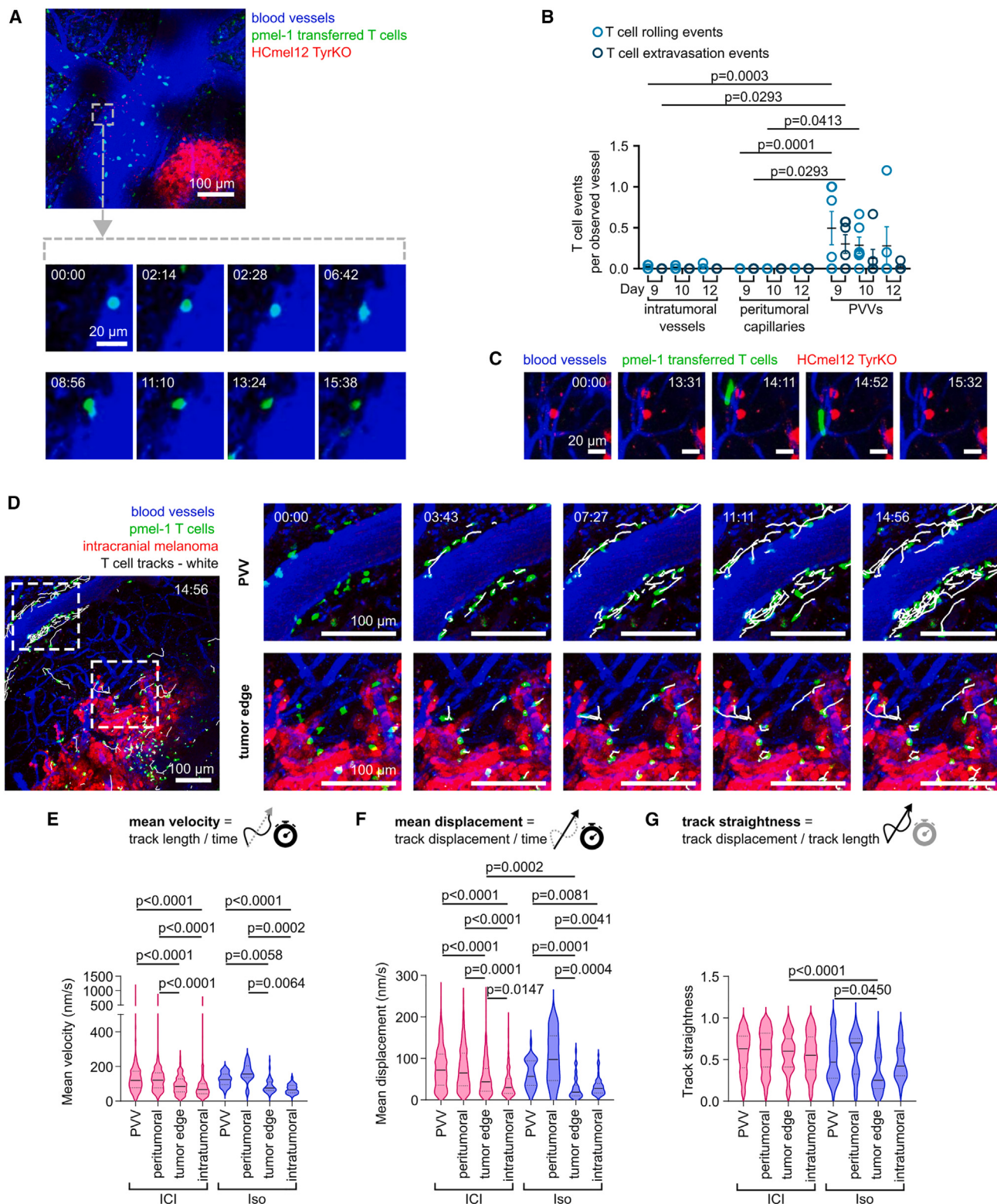


Figure 4. PVVs exhibit increased T cell motility and are the sites of T cell extravasation

(A) IVM time series images of a pmel-1 T cell extravasation from a PVV of ICI-treated HCmel12 TyrKO intracranial melanoma on day 12 post TI 4 days post ACT over a time course of 17:52 min. Overview image (MIP of 90 μm depth), zoom on time series images (single z-planes).

(B) Quantification of T cell rolling (intraluminal retention for >2 min) and T cell extravasation events of pmel-1 T cells at distinct vessels of ICI-treated intracranial HCmel12 TyrKO depicted as T cell events per observed vessel on days 9, 10, and 12 post TI. Due to the very low abundance of T cells at the sagittal sinus, this

(legend continued on next page)

spectral flow cytometry of intracranial melanomas in LCK-Cre × LSL-tdTomato mice on day 10 post cortical TI (Figures 5 and S6). ICAM-1, but not VCAM-1, was highly expressed in endothelial cells (Figure 5A) and ICAM-1 also, relevantly, from pericytes (Figure 5B) in the brain tumor hemisphere. ICI treatment did not significantly affect ICAM-1 or VCAM-1 expression on endothelial cells (Figure 5A), while it increased ICAM-1 and VCAM-1 expression on pericytes (Figure 5B). Nevertheless, on endothelial cells, ICAM-1 expression (but not VCAM-1 expression) was moderately increased in the tumor and its microenvironment as compared with the contralateral non-tumor hemisphere (Figures 5C and 5D). On pericytes, ICAM-1 expression was even more robustly increased in the tumor hemisphere as compared with the non-tumor hemisphere (Figures 5E and 5F), and the low pericytic VCAM-1 expression also somewhat increased after ICI treatment in the tumor hemisphere (Figure 5F). Analysis of surface markers of other major immune cell subpopulations revealed that the tumor-bearing hemisphere was mainly infiltrated by microglia, T cells, and macrophages, while other immune cell types such as granulocytes, B cells, DCs, and NK cells could only be detected at very low frequencies (Figures 5G and 5H). ICI treatment significantly increased the percentage of LFA-1, PD-1 double-positive CD4⁺ T cells (Figure 5I), with a similar trend in CD8⁺ T cells (Figure 5J). Together, these data support a mechanism where regionally increased ICAM-1 expression in two main cell types of the vascular wall and, potentially, other cell types that were not investigated here, attracts a higher numbers of activated T cells that express the ICAM-1 ligand LFA-1, resulting in increased T cell entry into the brain and efficient recruitment to intracranial melanoma tumors, particularly under ICI treatment.

Finally, to provide further evidence for the relationship of ICAM-1 expression of PVVs and T cell recruitment at this very site, we performed longitudinal IVM of intraluminal ICAM-1 expression by *in vivo* immunostaining through intravenous injection of a fluorescent anti-ICAM-1 antibody (Figures 6A–6D). These experiments confirmed that high ICAM-1 signals were detectable at the endothelial lining of PVVs (Figure 6E), specifically at those PVVs where also a high abundance and dynamics of perivascular T cells could be observed, while PVV regions with less T cell accumulation exhibited less ICAM-1 staining (Figures 6A–6F; Video S6). No such relation was detectable at brain surface capillaries and no correlation with vascular diameter was observed (Figures 6G–6I), and an intravenous (i.v.) injection of a fluorescein isothiocyanate (FITC)-coupled Iso control antibody did not result in signal accumulation above background at PVVs and other vessel types (Figures S7A–S7C). All in all, vascular ICAM-1 expression at PVVs was associated with efficient T cell recruitment to intracranial melanoma tumors, particularly under ICI treatment.

region was not included in the analysis. Two-way ANOVA with Tukey's post hoc test, dots represent individual mice, for numbers of observed mice and vessels see Table S1.

(C) IVM time series images (MIPs of 70 μm depth) of a pmel-1 T cell (green) 4 h post ACT flushed through a peritumoral capillary (blue) without stable vascular attachment on day 8 post TI of HCmel12 TyrKO intracranial melanoma (red) treated with ICI.

(D) IVM time series images of T cells at day 10 post TI under ICI treatment over a period of 15 min showing T cell tracks at a PVV and at the tumor edge as indicated in an overview image (MIP) and in higher magnifications (MIPs).

(E–G) Violin plots of T cell mean velocity (E), mean displacement (F), and track straightness (G) of motile transferred T cells comparing different regions on day 10 post TI under ICI and control treatment. *p* values were calculated using Kruskal-Wallis test with Dunn's post hoc test, *n* = 4 mice per group, black bars represent medians, dotted lines represent quartiles. Intravenously injected TRITC-dextran (blue) shows the vessel lumens (in A, C, and D).

ICAM-1 is required for efficient T cell recruitment to PVVs and antitumor immunity

To validate the functional relevance of ICAM-1 for ICI-mediated T cell recruitment to the brain, ICAM-1 was functionally blocked *in vivo* by i.v. injection of a neutralizing anti-ICAM-1 antibody or Iso control into intracranial and extracranial HCmel12 TyrKO-melanoma-bearing mice, and brain tumor growth and T cell infiltration were analyzed by IVM. ICAM-1 blocking had no relevant effect on extracranial-flank tumor growth (Figure 6J). In contrast, ICI-treatment-induced complete regression of brain tumor growth was substantially attenuated by ICAM-1 blockade (Figure 6K). Brain infiltration of T cells closely localized at PVVs at day 5, an early time point important for the recruitment of activated T cells, was significantly reduced under anti-ICAM-1 blockade (Figure 6L). In summary, while additional effects of ICAM-1 blockade on tumor growth in the brain might also contribute, these findings suggest that specific molecular features of PVVs, particularly high ICAM-1 expression that allows vascular adhesion and extravasation of circulating T cells, are responsible for efficient T cell recruitment to brain tumors as a prerequisite for their antitumor activity.

ICAM-1 expression on PVVs correlates with T cell infiltration in human brain metastases

Finally, to elucidate the expression patterns of *ICAM-1* in patients with brain metastases, we first analyzed single-cell RNA sequencing datasets published by Gonzalez et al.²³ This study characterized the tumor microenvironment of brain metastases in patients, providing well-defined transcriptional profiles of three distinct endothelial cell populations with arterial mixed/capillary (EC-1), venous (EC-2), or arterial (EC-3) phenotype in the brain.²³ Further *in silico* analyses of these datasets revealed expression of ICAM-1 on endothelial cells (EC-1–3) in brain tumors of all entities, with particularly high *ICAM-1* expression in the venous EC-2 cell population of breast and lung cancer brain metastasis (Figure 7A). In melanoma samples, highest expressions could be observed in both venous and arterial ECs, while all other cell populations exhibited only low *ICAM-1* expression (Figures 7A and 7B). *ICAM-1* expression of the venous EC-2 cell population was, however, heterogeneous in all entities (Figure 7B), which would be consistent with a situation where only a fraction of venous ECs, like those found in PVVs, relevantly express *ICAM-1*.

Next, we set out to investigate whether these higher *ICAM-1* expression levels could indeed come from PVV structures, consistently found in the mouse models investigated, in the human disease. Multiparametric immunofluorescence staining was performed on tissues of ten patients with melanoma brain metastases where both solid tumor tissue and adjacent brain tissue

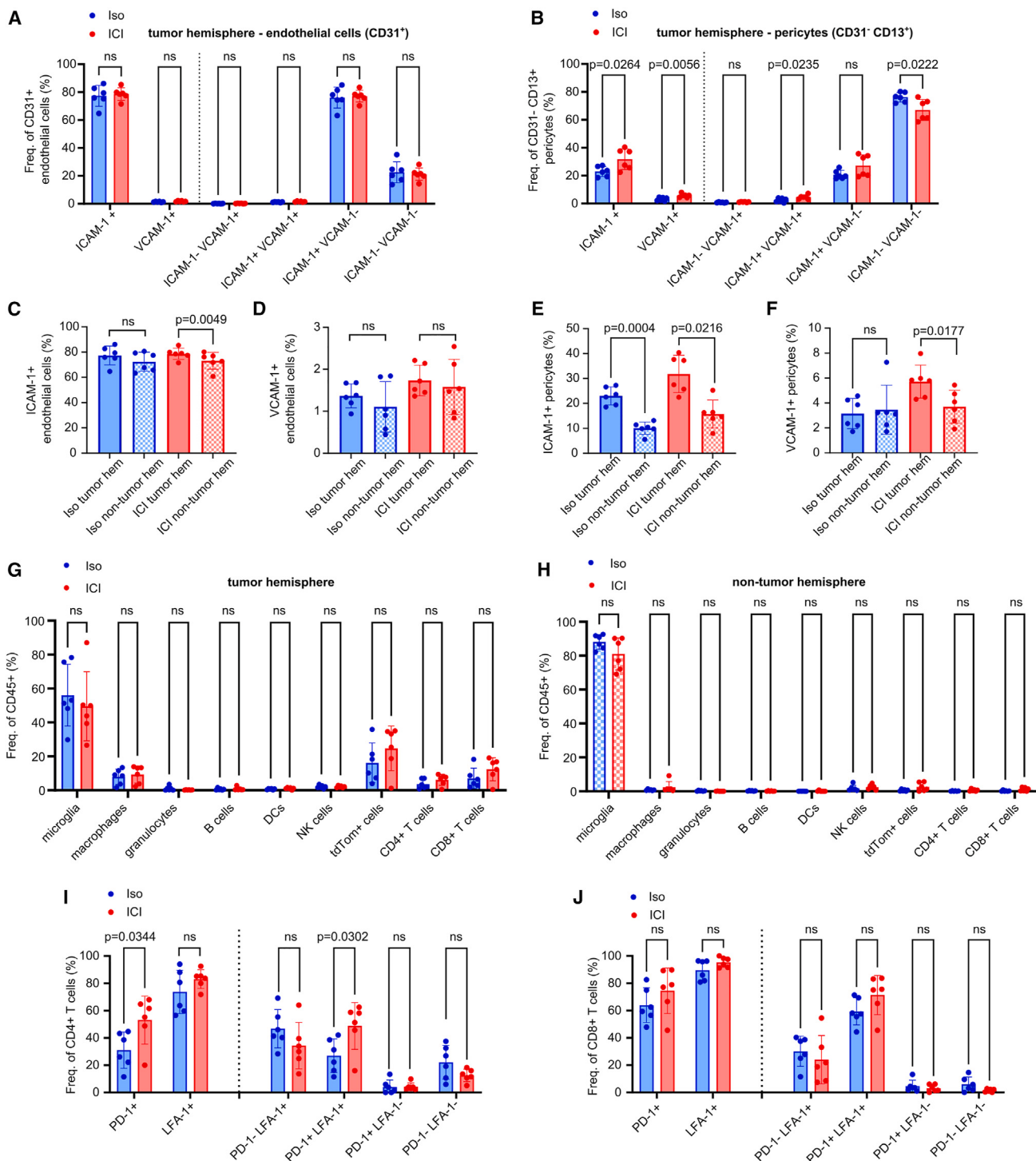


Figure 5. Flow cytometry analysis of vascular and immune cells in intracranial melanoma under ICI

(A and B) Spectral flow cytometry analysis of LCK-Cre × LSL-tdTomato mice with HCmel12 TyrKO GFP brain tumors on day 10 post cortical injection under ICI or isotype control treatment. Frequencies of ICAM-1, and VCAM-1 single-positive or ICAM-1 VCAM-1 double-positive cell populations were quantified as frequencies of CD31⁺ endothelial cells (A) in the tumor hemisphere, as frequencies of CD13⁺ pericytes in the tumor hemisphere (B).

(C–F) Endothelial (C and D) or pericytic (E and F) ICAM-1 expression (C and E) and VCAM-1 expression (D and F) from the tumor-bearing hemisphere (also shown in the first four bars of A and B) was compared with the data from the non-tumor hemisphere.

(legend continued on next page)

were preserved in the specimen (Figures 7C–7F). In all ten patients, we were able to detect ICAM-1 expression on peritumoral blood vessels (Figures 7C and 7D), in accordance with our findings from the preclinical models. The majority of large venous vessels, but only a small proportion of peritumoral capillaries, stained positive for ICAM-1 (Figure 7D). The extent of intratumoral T cell infiltration correlated with ICAM-1 positivity of the PVV-like large venous vessels in the peritumoral region, reaching statistical significance only for this vessel type (Figures 7E and 7F). In accordance with our findings from the mouse models of melanoma brain tumors, PVV-like vessels could also be identified in samples of human brain metastases and ICAM-1 positivity of these vessels was also associated with T cell recruitment to the brain tumors.

DISCUSSION

In this study we dynamically investigated the interplay of T cell infiltration and melanoma brain tumor growth in real time over prolonged periods of time using two mouse models that we generated. This revealed a specific T cell brain entry and tumor homing mechanism via distinct anatomical structures, PVVs. Mechanistically, the leukocyte adhesion molecule ICAM-1, highly expressed at the endothelial lining of T cell-rich PVVs and increased also in brain pericytes and potentially other cells in the tumor microenvironment after checkpoint blockade, drives PVV-related T cell homing to brain tumors, facilitating their full antitumor activity. Similar PVV-like structures could also be found at the interface between the brain metastasis and brain in cancer patients.

The mechanisms of T cell surveillance of the healthy brain¹⁴ differ from T cell recruitment to brain tumors: in the brain tumor setting, we neither observed T cell recruitment from the sagittal sinus area (the place of lymphatic structures in the brain^{4,5}) nor from leaky, strongly pathologic tumor microvessels^{24,25} but exclusively at pre-existing large venous vessels that we have termed PVVs in this tumor context. In accordance with our study, the general importance of blood vessels for immunotherapy of brain tumors has recently been demonstrated by a preclinical study of glioblastoma²⁶. Ma et al. have shown that vascular normalization by targeting p21-activated kinase 4 (PAK4), and thereby increasing the vascular expression of adhesion molecules, including ICAM-1, in a preclinical model of glioblastoma, can improve chimeric antigen receptor T cell immunotherapy. The discovery of PVVs reported here can also help to explain how meningeal vessels at the brain surface can become a critical place for the neuroimmune interface,^{14,27–29} here in the context of antitumor immunity in the brain. However, we also demonstrate here that PVV structures are not limited to the brain surface.

Different tissue architecture in different organs provides a variability of structures that can be exploited as guidance, or represent challenges, for immune cell recruitment to reach their target site. Especially, extracellular matrix components³⁰ and blood vessels³¹ were shown to be used as guiding paths for immune

cells to reach their destinations, such as for guiding T cells to T cell zones in the spleen. It is therefore conceivable that PVVs in the brain provide similar structures. It has been shown recently that myeloid cells derived from the bone-marrow niche adjacent to the brain and spinal cord can migrate through meningeal barriers to the brain parenchyma under inflammatory conditions.³² Whether PVVs could act as a scaffold for facilitating migration of these myeloid cells to brain tumors, or whether the bone-marrow niche could also supply lymphocytes to the brain via these routes, remains to be elucidated.

Intravital multi-photon imaging has recently proven to be a powerful tool to elucidate lymphocyte migration within inflamed lymph nodes³³ as well as the dynamics of antitumor immunity in the living animal, for example, by visualization of spreading of T cell-derived interferon (IFN)-γ and its effect on tumor cells.³⁴ Specifically, a balanced regulation of T cell motility and dynamics is important for efficient T cell activation and the ability to conduct antitumor effector functions. This has been studied in short-term experiments using *in vivo* and *ex vivo* imaging for different aspects of T cell function, such as circulating to and within secondary lymphoid organs,^{18,31,35,36} antigen recognition at antigen-presenting cells in lymphoid organs,³⁷ migration and extravasation from the blood,³⁸ trafficking to and within an extracranial tumor,^{16,17,30,39,40} and engaging with extracranial tumor target cells.^{17,41–44} Concluding from these studies, T cell motility seems to be regulated depending on the context. During antigen search and migration phases in the tumor periphery and during migration to lymphoid organs, T cell motility is high. For allowing efficient antigenic contacts at antigen-presenting cells in lymphoid organs or at target cells, T cell motility decreases to allow the formation of stable immune synapses and stable interactions with antigen presented on target cells. In line with these previous imaging studies of extracranial solid tumors, our work demonstrates the importance of a distinct interpretation of T cell movement patterns and motility features, depending on their localization and stage in the cancer-immunity cycle.⁴⁵ Gaining more insight into these major immune functions within the brain is important to understand the prerequisites for effective intracranial immune responses and, subsequently, for the development of better therapeutic strategies for the treatment of brain tumors.

It has been demonstrated before that CTLA-4 expression could affect T cell migration and motility in seemingly contrasting ways. CTLA-4 has been shown to interfere with T cell activation by limiting T cell dwell times at antigen-presenting cells *ex vivo*^{46–50}; however, increased T cell velocities were also associated with successful anti-CTLA-4 immunotherapy in extracranial melanoma.¹⁸ Moreover, *in vivo* microscopy revealed that anti-PD-1/programmed death-ligand 1 (PD-L1) therapy restored CD8⁺ T cell motility in the spleen following persistent viral-infection-induced exhaustion.⁵¹

The results of this study also point toward potential strategies to improve immunotherapies for brain cancer. One strategy could be to further increase ICAM-1-dependent T cell homing to the brain by specific extracranial T cell priming,¹² including

(G and H) Infiltrating immune cell populations were quantified as frequencies of CD45⁺ cells under ICI treatment of isotype control treatment for the tumor hemisphere (G) and the non-tumor hemisphere (H).

(I and J) PD-1 and LFA-1 expression of CD4⁺ T cells (I) and CD8⁺ T cells (J) were quantified in the tumor hemisphere. For statistical analysis multiple unpaired t tests were used, $n = 6$ mice per group. See also Figures S5 and S6.

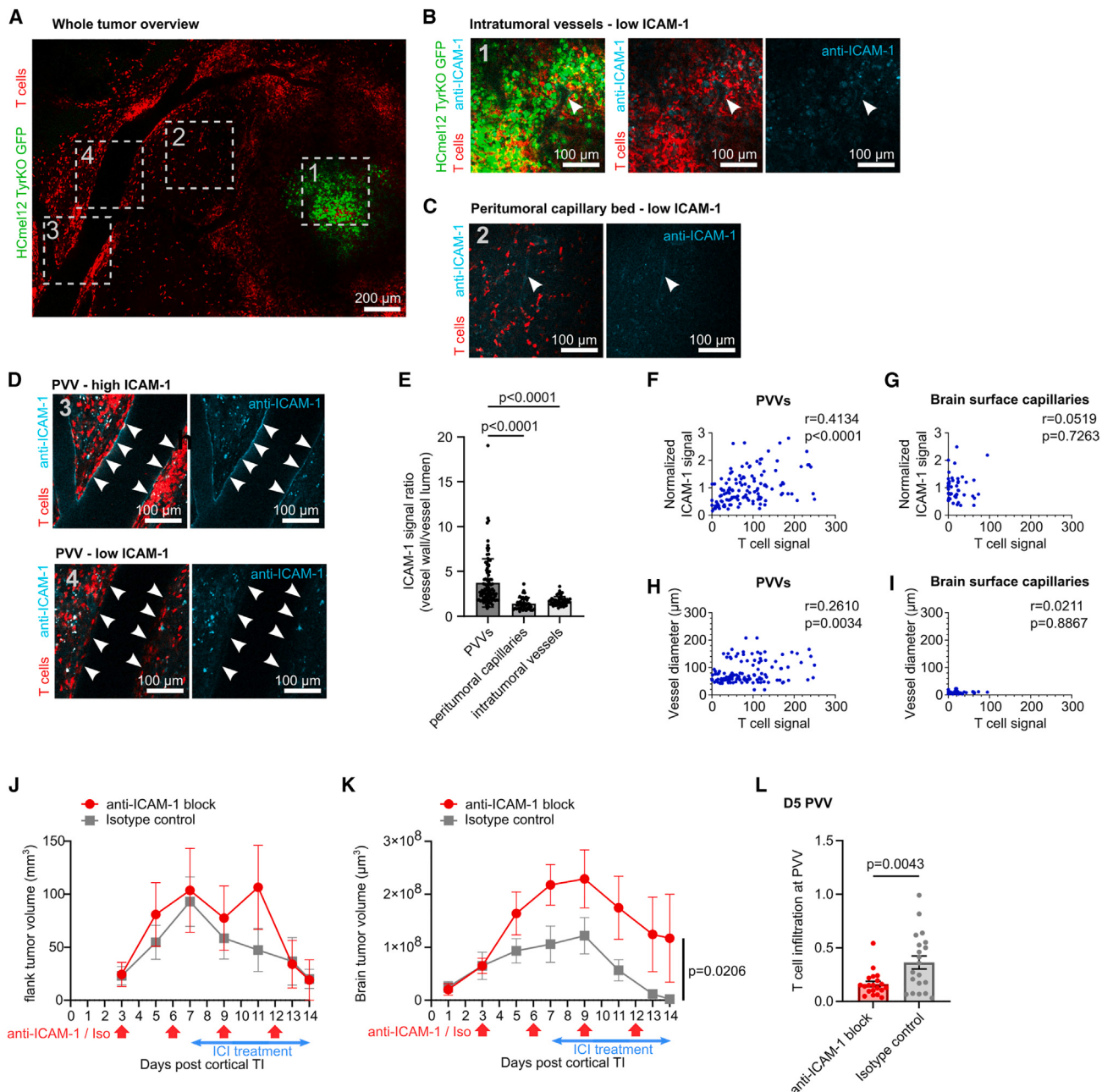


Figure 6. ICAM-1 fosters T cell recruitment at PVVs and antitumor immunity

IVM of *in vivo* ICAM-1 staining of intracranial HCmel12 TyrKO-melanoma-bearing LCK-Cre × LSL-TdTomato mice treated with ICI, at day 10 post TI. (A–D) IVM of the intracranial tumor and its periphery before anti-ICAM-1 FITC injection (A) and 1–3 h after anti-ICAM-1 injection (B–D). Numbered boxes indicate distinct regions shown in higher magnification, such as an intratumoral region (B) the peritumoral capillary bed (C), and regions at a PVV with high and low ICAM-1 signal (D). Arrows indicate the position of the vessel walls of the respective vessel types. Field of views are corresponding to numbered boxes (A).

(E) Quantification of ICAM-1 intensity of PVVs, peritumoral capillaries close to the brain surface and intratumoral vessels shown as ratio of ICAM-1 intensity at the vessel wall/ICAM-1 intensity in the respective vessel lumen from $n = 3$ mice, Kruskal-Wallis test with Dunn's multiple comparisons test.

(F–I) T cell signal intensities in the perivascular space at 30 μm distance from the vessel walls (x axis) are plotted against normalized intraluminal ICAM-1 signal intensities (y axis) at different positions at PVVs (F), and at brain surface capillaries (G), and against the corresponding vessel diameters (y axis) of each position on PVVs (H) and on brain surface capillaries (I). Linear regression, $n = 3$ mice.

(J–L) IVM analysis of functional ICAM-1 blocking *in vivo* by i.v. injection of anti-ICAM-1 or isotype control antibodies starting from day 3 post cortical TI in ICI-treated HCmel12 TyrKO intracranial- and extracranial-melanoma-bearing mice. $n = 6$ mice injected with anti-ICAM-1, $n = 8$ mice injected with isotype control.

(legend continued on next page)

vaccination approaches. For the application of cellular therapies, such as chimeric antigen receptor (CAR)-T cell therapies or T cell receptor (TCR)-T cell therapies, it might be beneficial to engineer these cells to express elevated levels of the ICAM-1 ligand LFA-1 to better equip them for brain homing. Those strategies can be tested.

All in all, our study indicates that, in brain tumors, increased T cell motility under ICI treatment is beneficial for intracranial antitumor immunity as it enables T cells to extravasate at PVVs via an ICAM-1-guided mechanism and exploit the PVV perivascular space as a fast track within the brain for efficient homing to the intracranial tumor. Thus, the discovery and characterization of PVVs as an exquisite site of T cell recruitment helped to decipher key features of antitumor immunity against melanoma brain tumors; it is exciting to learn whether this mechanism also applies to other malignancies in the brain and beyond. Last but not least, those insights can be used to develop improved antitumor immunotherapies.

Limitations of the study

Our study unravels T cell motility patterns in real time and over several days in a living animal, in cancer and in the brain. Although signs of surgery-induced inflammation were minimal in our experiment, we cannot fully exclude that T cell trafficking might have been altered to some extent by the surgical procedures necessary to achieve intravital imaging of the brain. However, the additional murine and human immunohistological studies conducted here confirmed that T cell-rich PVV structures can be found around many melanoma brain tumors, independent of prior surgery. As pmel-1 T cells recognize melanocytic antigens, adoptive transfer in C57BL/6 mice might also lead to off-tumor autoreactive responses. Although signs of autoimmunity, i.e., loss of skin pigmentation, were not observed upon pmel-1 ACT, we cannot completely exclude ACT-mediated off-tumor effects. Only male mice were used for *in vivo* experiments in this study; therefore, it is unclear whether the findings presented here can be fully generalized to both sexes. Finally, this study demonstrates the expression of ICAM-1 on endothelial cells and pericytes, but future studies are required to study how ICI alters expression of ICAM-1 on other cell types, such as myeloid cells, and how this effects T cell dynamics and antitumor response.

RESOURCE AVAILABILITY

Lead contact

Further information and requests for resources and reagents should be directed to and will be fulfilled by the lead contact, Frank Winkler (frank.winkler@med.uni-heidelberg.de).

Materials availability

This study did not generate new unique reagents.

Data and code availability

- This paper analyzes existing, publicly available data. The accession number for the dataset is listed in the [key resources table](#).

- This paper does not report original code.
- Any additional information required to reanalyze the data reported in this paper is available from the [lead contact](#) upon reasonable request.

ACKNOWLEDGMENTS

We thank T. Tütting and J. Landsberg for kindly sharing the HCmel12 cell line with us and V. Umansky for the Ret cell line. We also thank D. Tschaharganeh and A. Martin-Villalba for providing mouse lines to establish breeding of the LCK-Cre × LSL-tdTomato mice. We also thank M. Platten for providing pmel-1 and OT-I mice. We thank Yvonne Yang for assisting with imaging experiments. We acknowledge the support of DKFZ Light Microscopy Facility (LMF) and DKFZ flow cytometry core facility. We would also like to thank the Flow Cytometry Core Facility of the Medical Faculty at the University of Bonn for providing help, services, and devices funded by the Deutsche Forschungsgemeinschaft (DFG, German Research foundation, Projektnummer: 471514137). This work was funded by the Deutsche Forschungsgemeinschaft (DFG, German Research Foundation) project number 259332240/RG 2099 (addressed to M.A.K. and F.W.) and supported by the Deutsche Krebsforschung (German Cancer Aid), Priority Program "Translational Oncology," #70112507, "Preventive strategies against brain metastases" (addressed to W.W. and F.W.). This work was supported by the Bundesministerium für Bildung und Forschung within the framework of the e:Med research and funding concept 01ZX1913A to D.W., 01ZX1913C to R.W., and 01ZX1913D to M.A.K. This work was also supported in part by the Deutsche Krebsforschung (German Cancer Aid) project grants 70113168 and 70114292 (Excellence Program) to M.H. and Deutsche Forschungsgemeinschaft (DFG, German Research Foundation) under Germany's Excellence Strategy—EXC2151—390873048 to M.H.

AUTHOR CONTRIBUTIONS

Conceptualization, F.W. and M.A.K.; methodology, J.M.M., C.T., M.P., C.D.M., R.W., D.W., V.V., M.E., M.S., A.S.B., I.H., D.S., D.H., and M.H.; investigation, J.M.M., C.T., M.P., V.V., M.S., R.W., and D.W.; visualization, J.M.M., M.P., and V.V.; funding acquisition, F.W., M.A.K., W.W., and M.H.; supervision, F.W. and M.A.K.; writing – original draft, J.M.M.; writing – review and editing, J.M.M., F.W., and M.A.K.

DECLARATION OF INTERESTS

F.W. reports receiving research grants from Boehringer, Genentech, Roche, and Divide and Conquer Ltd.

STAR METHODS

Detailed methods are provided in the online version of this paper and include the following:

- KEY RESOURCES TABLE
- EXPERIMENTAL MODEL AND STUDY PARTICIPANT DETAILS
 - Animals and surgical procedures
 - Chronic cranial window implantation
 - Flank tumor inoculation
 - Cortical and striatal tumor injection
 - Adoptive T cell transfer
 - In vivo* two-photon laser scanning microscopy (IVM)
 - Immune-checkpoint therapy
 - Monitoring of flank tumor size
 - Cell lines
 - Brain metastasis patient samples
- METHOD DETAILS
 - Immuno-blotting

Quantification of flank tumor growth (J), brain tumor volume (K), and T cell infiltration at PVVs on day 5 (binarized T cell volume within 30 µm surrounding the PVV/PVV vessel volume) (L). Each data point represents one PVV, treated with anti-ICAM-1 (red, left) or isotype control antibody (gray, right) (L). Statistical analysis was performed using a mixed-effects model (J and K), and unpaired t test on $n = 20$ PVVs per group of $n = 6$ mice anti-ICAM-1 and $n = 8$ mice isotype control (L). See also [Figure S7](#).

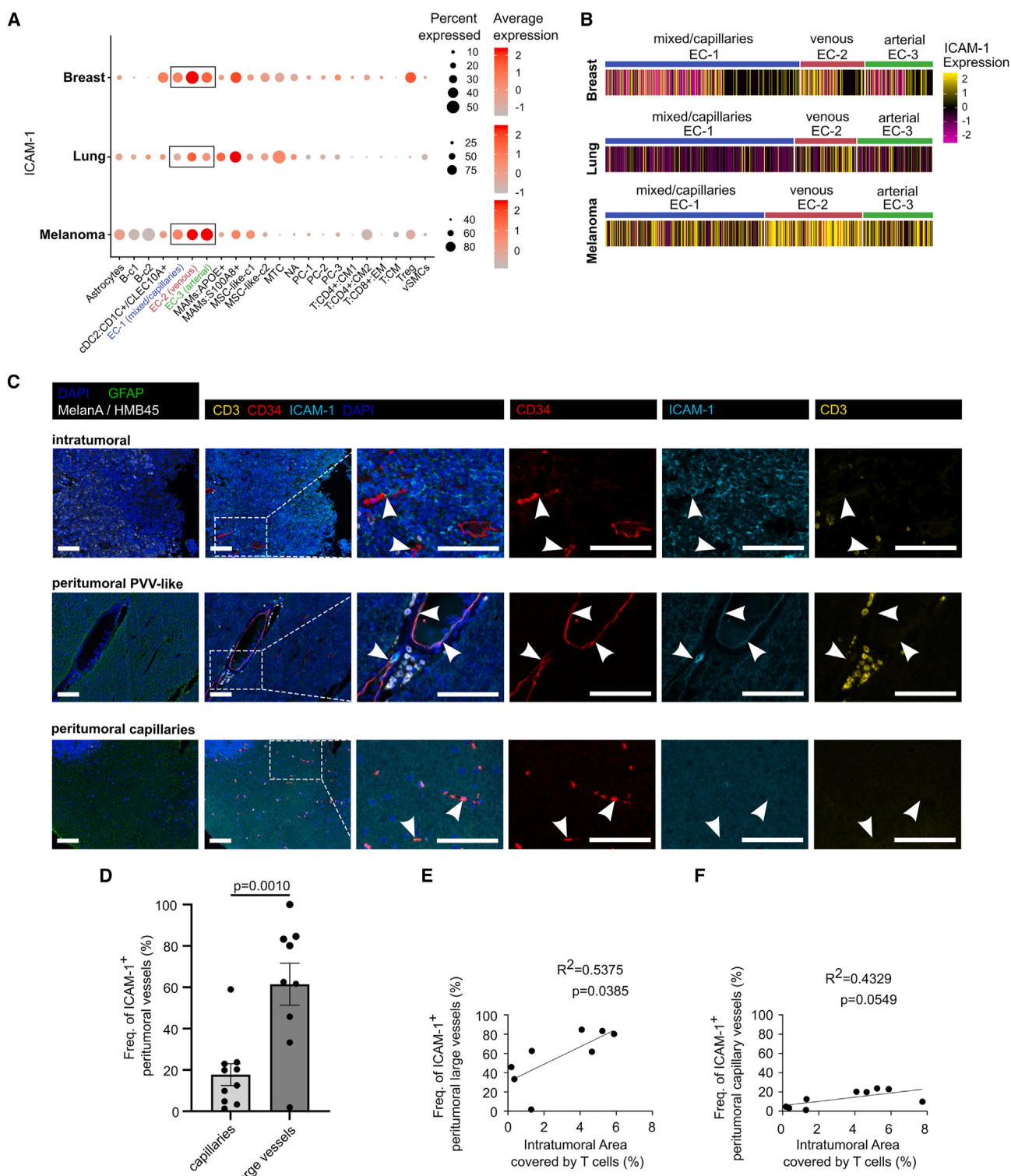


Figure 7. ICAM-1-positive blood vessel structures in human brain metastases

(A and B) *In silico* analysis of ICAM-1 expression from a single-cell mRNA sequencing dataset of human breast, lung cancer and melanoma brain metastasis samples.²³ (A) Dot plots of ICAM-1 expression of different brain metastasis-associated stromal cell types: astrocytes, B cells (B-c1, -c2) dendritic cells (cDC2:CD1C+CLEC10+), endothelial cells (EC-1, EC-2, EC-3), metastasis-associated macrophages (MAMMs), mesenchymal-stromal-cell-like cells (MSC-like-1, -2), metastatic tumor cells (MTC), (NA), pericytes (PC-1-3), T cells (T:CD8+:EM, T:CD4+:CM1, T:CD4+:CM2, Tregs, T:CM), and vascular smooth muscle cells (vSMCs). (B) Heatmap of ICAM-1 expression in all endothelial cells (EC-1, EC-2, and EC-3) of breast, lung, and melanoma brain metastasis samples.

(legend continued on next page)

- Flow Cytometry
- *In vivo* antibody staining
- *In vivo* functional ICAM-1 blocking
- Immunofluorescence
- Multiparametric immunofluorescence
- QUANTIFICATION AND STATISTICAL ANALYSIS
 - Image Processing and Quantification
 - Single cell RNA-sequencing analysis
 - Statistical Analysis

SUPPLEMENTAL INFORMATION

Supplemental information can be found online at <https://doi.org/10.1016/j.immuni.2024.09.003>.

Received: July 11, 2024

Revised: August 14, 2024

Accepted: September 6, 2024

Published: October 4, 2024

REFERENCES

1. Davies, M.A., Liu, P., McIntrye, S., Kim, K.B., Papadopoulos, N., Hwu, W.J., Hwu, P., and Bedikian, A. (2011). Prognostic factors for survival in melanoma patients with brain metastases. *Cancer* 117, 1687–1696. <https://doi.org/10.1002/cncr.25634>.
2. Rieth, J.M., Swami, U., Mott, S.L., Zanaty, M., Henry, M.D., Bossler, A.D., Greenlee, J.D., Zakharia, Y., Vanneste, M., Jennings, B., et al. (2021). Melanoma brain metastases in the era of targeted therapy and checkpoint inhibitor therapy. *Cancers* 13, 1489. <https://doi.org/10.3390/cancers13071489>.
3. Carson, M.J., Doose, J.M., Melchior, B., Schmid, C.D., and Ploix, C.C. (2006). CNS immune privilege: hiding in plain sight. *Immunol. Rev.* 213, 48–65. <https://doi.org/10.1111/j.1600-065X.2006.00441.x>.
4. Aspelund, A., Antila, S., Proulx, S.T., Karlsen, T.V., Karaman, S., Detmar, M., Wiig, H., and Alitalo, K. (2015). A dural lymphatic vascular system that drains brain interstitial fluid and macromolecules. *J. Exp. Med.* 212, 991–999. <https://doi.org/10.1084/jem.20142290>.
5. Louveau, A., Smirnov, I., Keyes, T.J., Eccles, J.D., Rouhani, S.J., Peske, J.D., Derecki, N.C., Castle, D., Mandell, J.W., Lee, K.S., et al. (2015). Structural and functional features of central nervous system lymphatic vessels. *Nature* 523, 337–341. <https://doi.org/10.1038/nature14432>.
6. Absinta, M., Ha, S.-K., Nair, G., Sati, P., Luciano, N.J., Palisoc, M., Louveau, A., Zaghloul, K.A., Pittaluga, S., Kipnis, J., et al. (2017). Human and nonhuman primate meninges harbor lymphatic vessels that can be visualized noninvasively by MRI. *eLife* 6, e29738. <https://doi.org/10.7554/eLife.29738>.
7. Goodman, J.R., Adham, Z.O., Woltjer, R.L., Lund, A.W., and Iliff, J.J. (2018). Characterization of dural sinus-associated lymphatic vasculature in human Alzheimer's dementia subjects. *Brain Behav. Immun.* 73, 34–40. <https://doi.org/10.1016/j.bbi.2018.07.020>.
8. Long, G.V., Atkinson, V., Lo, S., Sandhu, S., Guminski, A.D., Brown, M.P., Wilmett, J.S., Edwards, J., Gonzalez, M., Scolyer, R.A., et al. (2018). Combination nivolumab and ipilimumab or nivolumab alone in melanoma brain metastases: a multicentre randomised phase 2 study. *Lancet Oncol.* 19, 672–681. [https://doi.org/10.1016/S1470-2045\(18\)30139-6](https://doi.org/10.1016/S1470-2045(18)30139-6).
9. Tawbi, H.A., Forsyth, P.A., Algazi, A., Hamid, O., Hodin, F.S., Moschos, S.J., Khushalani, N.I., Lewis, K., Lao, C.D., Postow, M.A., et al. (2018). Combined nivolumab and ipilimumab in melanoma metastatic to the brain. *N. Engl. J. Med.* 379, 722–730. <https://doi.org/10.1056/NEJMoa1805453>.
10. Berry, S., Giraldo, N.A., Green, B.F., Cottrell, T.R., Stein, J.E., Engle, E.L., Xu, H., Ogurtsova, A., Roberts, C., Wang, D., et al. (2021). Analysis of multispectral imaging with the AstroPath platform informs efficacy of PD-1 blockade. *Science* 372, eaba2609. <https://doi.org/10.1126/science.aba2609>.
11. Song, E., Mao, T., Dong, H., Boisserand, L.S.B., Antila, S., Bosenberg, M., Alitalo, K., Thomas, J.-L., and Iwasaki, A. (2020). VEGF-C-driven lymphatic drainage enables immuno surveillance of brain tumours. *Nature* 577, 689–694. <https://doi.org/10.1038/s41586-019-1912-x>.
12. Taggart, D., Andreou, T., Scott, K.J., Williams, J., Rippaus, N., Brownlie, R.J., Ilett, E.J., Salmon, R.J., Melcher, A., and Lorger, M. (2018). Anti-PD-1/anti-CTLA-4 efficacy in melanoma brain metastases depends on extracranial disease and augmentation of CD8(+) T cell trafficking. *Proc. Natl. Acad. Sci. USA* 115, E1540–E1549. <https://doi.org/10.1073/pnas.1714089115>.
13. Kim, T.N., Goodwill, P.W., Chen, Y., Conolly, S.M., Schaffer, C.B., Liepman, D., and Wang, R.A. (2012). Line-scanning particle image velocimetry: an optical approach for quantifying a wide range of blood flow speeds in live animals. *PLoS One* 7, e38590. <https://doi.org/10.1371/journal.pone.0038590>.
14. Rustenhoven, J., Drieu, A., Mamuladze, T., de Lima, K.A., Dykstra, T., Wall, M., Papadopoulos, Z., Kanamori, M., Salvador, A.F., Baker, W., et al. (2021). Functional characterization of the dural sinuses as a neuroimmune interface. *Cell* 184, 1000–1016.e27. <https://doi.org/10.1016/j.cell.2020.12.040>.
15. Kawakami, N., Nägerl, U.V., Odoardi, F., Bonhoeffer, T., Wekerle, H., and Flügel, A. (2005). Live imaging of effector cell trafficking and autoantigen recognition within the unfolding autoimmune encephalomyelitis lesion. *J. Exp. Med.* 201, 1805–1814. <https://doi.org/10.1084/jem.20050011>.
16. Boissonnas, A., Fetler, L., Zeelenberg, I.S., Hugues, S.P., and Amigorena, S. (2007). In vivo imaging of cytotoxic T cell infiltration and elimination of a solid tumor. *J. Exp. Med.* 204, 345–356. <https://doi.org/10.1084/jem.20061890>.
17. Lau, D., Garçon, F., Chandra, A., Lechermann, L.M., Aloj, L., Chilvers, E.R., Corrie, P.G., Okkenhaug, K., and Gallagher, F.A. (2020). Intravital imaging of adoptive T-cell morphology, mobility and trafficking following immune checkpoint inhibition in a mouse melanoma model. *Front. Immunol.* 11, 1514. <https://doi.org/10.3389/fimmu.2020.01514>.
18. Pentcheva-Hoang, T., Simpson, T.R., Montalvo-Ortiz, W., and Allison, J.P. (2014). Cytotoxic T lymphocyte antigen-4 blockade enhances antitumor immunity by stimulating melanoma-specific T-cell motility. *Cancer Immunol. Res.* 2, 970–980. <https://doi.org/10.1158/2326-6066.CIR-14-0104>.
19. Bartholomäus, I., Kawakami, N., Odoardi, F., Schläger, C., Mijikovic, D., Ellwart, J.W., Klinkert, W.E.F., Flügel-Koch, C., Issekutz, T.B., Wekerle, H., et al. (2009). Effector T cell interactions with meningeal vascular structures in nascent autoimmune CNS lesions. *Nature* 462, 94–98. <https://doi.org/10.1038/nature08478>.
20. Kerfoot, S.M., and Kubes, P. (2002). Overlapping Roles of P-Selectin and α_4 Integrin to Recruit Leukocytes to the Central Nervous System in Experimental Autoimmune Encephalomyelitis. *J. Immunol.* 169, 1000–1006. <https://doi.org/10.4049/jimmunol.169.2.1000>.
21. Carman, C.V., and Martinelli, R. (2015). T lymphocyte–endothelial interactions: emerging understanding of trafficking and antigen-specific immunity. *Front. Immunol.* 6, 603. <https://doi.org/10.3389/fimmu.2015.00603>.

(C) Multiparametric immunofluorescence images of human melanoma brain metastasis samples stained for GFAP, MelanA/HMB45, and nuclei (DAPI) markers to distinguish intratumoral (top row) from peritumoral regions (bottom rows). CD34 and CD3 were stained to detect vessels and T cells. Arrow heads indicate distinct blood vessels. Tumor cells also express ICAM-1. Scale bars, 100 μ m.

(D–F) Quantification of multiparametric immunofluorescence images of human melanoma brain metastasis from $n = 10$ patients. (D) Frequency of ICAM-1+ capillaries and large vessels. Statistical test: paired t test. (E and F) Correlation by linear regression of intratumoral T cell infiltration with the frequency of ICAM-1+ positive peritumoral large vessels (E), and with the frequency of peritumoral ICAM-1+ capillaries (F).

22. Lyck, R., Reiss, Y., Gerwin, N., Greenwood, J., Adamson, P., and Engelhardt, B. (2003). T-cell interaction with ICAM-1/ICAM-2 double-deficient brain endothelium in vitro: the cytoplasmic tail of endothelial ICAM-1 is necessary for transendothelial migration of T cells. *Blood* 102, 3675–3683. <https://doi.org/10.1182/blood-2003-02-0358>.
23. Gonzalez, H., Mei, W., Robles, I., Hagerling, C., Allen, B.M., Hauge Okholm, T.L., Nanjaraj, A., Verbeek, T., Kalavacherla, S., van Gogh, M., et al. (2022). Cellular architecture of human brain metastases. *Cell* 185, 729–745.e20. <https://doi.org/10.1016/j.cell.2021.12.043>.
24. Lockman, P.R., Mittapalli, R.K., Taskar, K.S., Rudraraju, V., Gril, B., Bohn, K.A., Adkins, C.E., Roberts, A., Thorsheim, H.R., Gaasch, J.A., et al. (2010). Heterogeneous blood-tumor barrier permeability determines drug efficacy in experimental brain metastases of breast cancer. *Clin. Cancer Res.* 16, 5664–5678. <https://doi.org/10.1158/1078-0432.CCR-10-1564>.
25. Lyle, L.T., Lockman, P.R., Adkins, C.E., Mohammad, A.S., Sechrest, E., Hua, E., Palmieri, D., Liewehr, D.J., Steinberg, S.M., Kloc, W., et al. (2016). Alterations in pericyte subpopulations are associated with elevated blood-tumor barrier permeability in experimental brain metastasis of breast cancer. *Clin. Cancer Res.* 22, 5287–5299. <https://doi.org/10.1158/1078-0432.CCR-15-1836>.
26. Ma, W., Wang, Y., Zhang, R., Yang, F., Zhang, D., Huang, M., Zhang, L., Dorsey, J.F., Binder, Z.A., O'Rourke, D.M., et al. (2021). Targeting PAK4 to reprogram the vascular microenvironment and improve CAR-T immunotherapy for glioblastoma. *Nat. Cancer* 2, 83–97. <https://doi.org/10.1038/s43018-020-00147-8>.
27. Hsu, M., Laaker, C., Madrid, A., Herbath, M., Choi, Y.H., Sandor, M., and Fabry, Z. (2022). Neuroinflammation creates an immune regulatory niche at the meningeal lymphatic vasculature near the cribriform plate. *Nat. Immunol.* 23, 581–593. <https://doi.org/10.1038/s41590-022-01158-6>.
28. Rustenhoven, J. (2021). A privileged brain. *Science* 374, 548. <https://doi.org/10.1126/science.abf7122>.
29. Rustenhoven, J., and Kipnis, J. (2019). Bypassing the blood-brain barrier. *Science* 366, 1448–1449. <https://doi.org/10.1126/science.aay0479>.
30. Bougherara, H., Mansuet-Lupo, A., Alifano, M., Ngô, C., Damotte, D., Le Frère-Belda, M.-A., Donnadieu, E., and Peranzoni, E. (2015). Real-time imaging of resident T cells in human lung and ovarian carcinomas reveals how different tumor microenvironments control T lymphocyte migration. *Front. Immunol.* 6, 500. <https://doi.org/10.3389/fimmu.2015.00500>.
31. Chauveau, A., Pirgova, G., Cheng, H.W., De Martin, A., Zhou, F.Y., Wideman, S., Rittscher, J., Ludewig, B., and Arnon, T.I. (2020). Visualization of T cell migration in the spleen reveals a network of perivascular pathways that guide entry into T Zones. *Immunity* 52, 794–807.e7. <https://doi.org/10.1016/j.immuni.2020.03.010>.
32. Cugurra, A., Mamuladze, T., Rustenhoven, J., Dykstra, T., Beroshvili, G., Greenberg, Z.J., Baker, W., Papadopoulos, Z., Drieu, A., Blackburn, S., et al. (2021). Skull and vertebral bone marrow are myeloid cell reservoirs for the meninges and CNS parenchyma. *Science* 373, eabf7844. <https://doi.org/10.1126/science.abf7844>.
33. Choe, K., Hontani, Y., Wang, T., Hebert, E., Ouzounov, D.G., Lai, K., Singh, A., Béguin, W., Melnick, A.M., and Xu, C. (2022). Intravital three-photon microscopy allows visualization over the entire depth of mouse lymph nodes. *Nat. Immunol.* 23, 330–340. <https://doi.org/10.1038/s41590-021-01101-1>.
34. Hoekstra, M.E., Bornes, L., Dijkgraaf, F.E., Philips, D., Pardieck, I.N., Toebe, M., Thommen, D.S., van Rheenen, J., and Schumacher, T.N.M. (2020). Long-distance modulation of bystander tumor cells by CD8+ T-cell-secreted IFN-γ. *Nat. Cancer* 1, 291–301. <https://doi.org/10.1038/s43018-020-0036-4>.
35. Kanda, Y., Okazaki, T., and Katakai, T. (2021). Motility dynamics of T cells in tumor-draining lymph nodes: A rational indicator of antitumor response and immune checkpoint blockade. *Cancers* 13, 4616. <https://doi.org/10.3390/cancers13184616>.
36. Stein, J.V., Rot, A., Luo, Y., Narasimhaswamy, M., Nakano, H., Gunn, M.D., Matsuzawa, A., Quackenbush, E.J., Dorf, M.E., and von Andrian, U.H. (2000). The Cc chemokine Thymus-Derived Chemotactic Agent 4 (Tca-4, Secondary Lymphoid Tissue chemokine, 6ckine, Exodus-2) Triggers lymphocyte Function-Associated Antigen 1-Mediated Arrest of Rolling T lymphocytes in peripheral lymph node high endothelial venules. *J. Exp. Med.* 191, 61–76. <https://doi.org/10.1084/jem.191.1.61>.
37. Mempel, T.R., Henrickson, S.E., and von Andrian, U.H. (2004). T-cell priming by dendritic cells in lymph nodes occurs in three distinct phases. *Nature* 427, 154–159. <https://doi.org/10.1038/nature02238>.
38. Millán, J., Hewlett, L., Glyn, M., Toomre, D., Clark, P., and Ridley, A.J. (2006). Lymphocyte transcellular migration occurs through recruitment of endothelial ICAM-1 to caveola- and F-actin-rich domains. *Nat. Cell Biol.* 8, 113–123. <https://doi.org/10.1038/ncb1356>.
39. Mrass, P., Kinjyo, I., Ng, L.G., Reiner, S.L., Puré, E., and Weninger, W. (2008). CD44 mediates successful interstitial navigation by killer T cells and enables efficient antitumor immunity. *Immunity* 29, 971–985. <https://doi.org/10.1016/j.immuni.2008.10.015>.
40. Peranzoni, E., Lemoine, J., Vimeux, L., Feuillet, V., Barrin, S., Kantari-Mimoun, C., Bercovici, N., Guérin, M., Biton, J., Ouakrim, H., et al. (2018). Macrophages impede CD8 T cells from reaching tumor cells and limit the efficacy of anti-PD-1 treatment. *Proc. Natl. Acad. Sci. USA* 115, E4041–E4050. <https://doi.org/10.1073/pnas.1720948115>.
41. Breart, B., Lemaître, F., Celli, S., and Bousso, P. (2008). Two-photon imaging of intratumoral CD8+ T cell cytotoxic activity during adoptive T cell therapy in mice. *J. Clin. Invest.* 118, 1390–1397. <https://doi.org/10.1172/JCI34388>.
42. Deguine, J., Breart, B., Lemaître, F., Di Santo, J.P., and Bousso, P. (2010). Intravital imaging reveals distinct dynamics for natural killer and CD8(+) T cells during tumor regression. *Immunity* 33, 632–644. <https://doi.org/10.1016/j.immuni.2010.09.016>.
43. Mrass, P., Takano, H., Ng, L.G., Daxini, S., Lasaro, M.O., Iparraguirre, A., Cavanagh, L.L., von Andrian, U.H., Ertl, H.C.J., Haydon, P.G., et al. (2006). Random migration precedes stable target cell interactions of tumor-infiltrating T cells. *J. Exp. Med.* 203, 2749–2761. <https://doi.org/10.1084/jem.20060710>.
44. Park, S.L., Buzzai, A., Rautela, J., Hor, J.L., Hochheiser, K., Effern, M., McBain, N., Wagner, T., Edwards, J., McConville, R., et al. (2019). Tissue-resident memory CD8+ T cells promote melanoma-immune equilibrium in skin. *Nature* 565, 366–371. <https://doi.org/10.1038/s41586-018-0812-9>.
45. Chen, D.S., and Mellman, I. (2013). Oncology meets immunology: the cancer-immunity cycle. *Immunity* 39, 1–10. <https://doi.org/10.1016/j.immuni.2013.07.012>.
46. Brunner-Weinzierl, M.C., and Rudd, C.E. (2018). CTLA-4 and PD-1 control of T-cell motility and migration: implications for tumor immunotherapy. *Front. Immunol.* 9, 2737. <https://doi.org/10.3389/fimmu.2018.02737>.
47. Rudd, C.E. (2008). The reverse stop-signal model for CTLA4 function. *Nat. Rev. Immunol.* 8, 153–160. <https://doi.org/10.1038/nri2253>.
48. Ruocco, M.G., Pilones, K.A., Kawashima, N., Cammer, M., Huang, J., Babb, J.S., Liu, M., Formenti, S.C., Dustin, M.L., and Demaria, S. (2012). Suppressing T cell motility induced by anti-CTLA-4 monotherapy improves antitumor effects. *J. Clin. Invest.* 122, 3718–3730. <https://doi.org/10.1172/JCI61931>.
49. Schneider, H., Downey, J., Smith, A., Zinselmeyer, B.H., Rush, C., Brewer, J.M., Wei, B., Hogg, N., Garside, P., and Rudd, C.E. (2006). Reversal of the TCR stop signal by CTLA-4. *Science* 313, 1972–1975. <https://doi.org/10.1126/science.1131078>.
50. Schneider, H., Smith, X., Liu, H., Bismuth, G., and Rudd, C.E. (2008). CTLA-4 disrupts ZAP70 microcluster formation with reduced T cell/APC dwell times and calcium mobilization. *Eur. J. Immunol.* 38, 40–47. <https://doi.org/10.1002/eji.200737423>.
51. Zinselmeyer, B.H., Heydari, S., Sacristán, C., Nayak, D., Cammer, M., Herz, J., Cheng, X., Davis, S.J., Dustin, M.L., and McGavern, D.B. (2013). PD-1 promotes immune exhaustion by inducing antiviral T cell motility paralysis. *J. Exp. Med.* 210, 757–774. <https://doi.org/10.1084/jem.20121416>.

52. Bald, T., Quast, T., Landsberg, J., Rogava, M., Glodde, N., Lopez-Ramos, D., Kohlmeyer, J., Riesenbergs, S., van den Boorn-Konijnenberg, D., Hömig-Hölzel, C., et al. (2014). Ultraviolet-radiation-induced inflammation promotes angiogenesis and metastasis in melanoma. *Nature* 507, 109–113. <https://doi.org/10.1038/nature13111>.
53. Overwijk, W.W., Theoret, M.R., Finkelstein, S.E., Surman, D.R., de Jong, L.A., Vyth-Dreese, F.A., Delleijn, T.A., Antony, P.A., Spiess, P.J., Palmer, D.C., et al. (2003). Tumor regression and autoimmunity after reversal of a functionally tolerant state of self-reactive CD8+ T cells. *J. Exp. Med.* 198, 569–580. <https://doi.org/10.1084/jem.20030590>.
54. Hogquist, K.A., Jameson, S.C., Heath, W.R., Howard, J.L., Bevan, M.J., and Carbone, F.R. (1994). T cell receptor antagonist peptides induce positive selection. *Cell* 76, 17–27. [https://doi.org/10.1016/0092-8674\(94\)90169-4](https://doi.org/10.1016/0092-8674(94)90169-4).
55. Hennet, T., Hagen, F.K., Tabak, L.A., and Marth, J.D. (1995). T-cell-specific deletion of a polypeptide N-acetylgalactosaminyl-transferase gene by site-directed recombination. *Proc. Natl. Acad. Sci. USA* 92, 12070–12074. <https://doi.org/10.1073/pnas.92.26.12070>.
56. Madisen, L., Zwingman, T.A., Sunkin, S.M., Oh, S.W., Zariwala, H.A., Gu, H., Ng, L.L., Palmiter, R.D., Hawrylycz, M.J., Jones, A.R., et al. (2010). A robust and high-throughput Cre reporting and characterization system for the whole mouse brain. *Nat. Neurosci.* 13, 133–140. <https://doi.org/10.1038/nn.2467>.
57. Berg, S., Kutra, D., Kroeger, T., Straehle, C.N., Kausler, B.X., Haubold, C., Schiegg, M., Ales, J., Beier, T., Rudy, M., et al. (2019). ilastik: interactive machine learning for (bio)image analysis. *Nat. Methods* 16, 1226–1232. <https://doi.org/10.1038/s41592-019-0582-9>.
58. Schindelin, J., Arganda-Carreras, I., Frise, E., Kaynig, V., Longair, M., Pietzsch, T., Preibisch, S., Rueden, C., Saalfeld, S., Schmid, B., et al. (2012). Fiji: an open-source platform for biological-image analysis. *Nat. Methods* 9, 676–682. <https://doi.org/10.1038/nmeth.2019>.
59. Kienast, Y., von Baumgarten, L., Fuhrmann, M., Klinkert, W.E.F., Goldbrunner, R., Herms, J., and Winkler, F. (2010). Real-time imaging reveals the single steps of brain metastasis formation. *Nat. Med.* 16, 116–122. <https://doi.org/10.1038/nm.2072>.
60. Zhang, X.-W., Huck, K., Jähne, K., Cichon, F., Sonner, J.K., Ufer, F., Bauer, S., Woo, M.S., Green, E., Lu, K., et al. (2021). Activity-regulated cytoskeleton-associated protein/activity-regulated gene 3.1 (Arc/Arg3.1) enhances dendritic cell vaccination in experimental melanoma. *Oncogene* 40, 1920739. <https://doi.org/10.1080/2162402X.2021.1920739>.
61. Valiente, M., Van Swearingen, A.E.D., Anders, C.K., Bairoch, A., Boire, A., Bos, P.D., Cittelly, D.M., Erez, N., Ferraro, G.B., Fukumura, D., et al. (2020). Brain metastasis cell lines panel: A public resource of organotropic cell lines. *Cancer Res.* 80, 4314–4323. <https://doi.org/10.1158/0008-5472.CAN-20-0291>.
62. Hao, Y., Hao, S., Andersen-Nissen, E., Mauck, W.M., Zheng, S., Butler, A., Lee, M.J., Wilk, A.J., Darby, C., Zager, M., et al. (2021). Integrated analysis of multimodal single-cell data. *Cell* 184, 3573–3587.e29. <https://doi.org/10.1016/j.cell.2021.04.048>.

STAR★METHODS
KEY RESOURCES TABLE

REAGENT or RESOURCE	SOURCE	IDENTIFIER
Antibodies		
CD279 (PD-1) Monoclonal Antibody (J43), PE	Thermo Fisher Scientific	Cat#12-9985-83; RRID: AB_466296; Lot#E0231-1634
PE/Cyanine7 anti-mouse CD3 Antibody, clone 17A2	BioLegend	Cat#100220; RRID: AB_1732057; Lot#B185661
CD8a Monoclonal Antibody (53-6.7), PerCP-Cyanine5.5	Thermo Fisher Scientific	Cat#2151510; RRID:AB_1107004; Lot#2151510
Pacific Blue™ anti-mouse CD4 Antibody, clone RM4-5	BioLegend	Cat#100531; RRID: AB_493374; Lot# B255834
Brilliant Violet 510™ anti-mouse/human CD44 Antibody, clone IM7	BioLegend	Cat#103044; RRID: AB_2650923; Lot# B227210
CD69 Monoclonal Antibody (H1.2F3), APC	Thermo Fisher Scientific	Cat#17-0691-82; RRID: AB_1210795; Lot#2065643
CD4 Monoclonal Antibody (GK1.5), FITC	Thermo Fisher Scientific	Cat#11-0041-85; RRID: AB_464893; Lot#1987705
Brilliant Violet 421™ anti-mouse CD366 (Tim-3) Antibody, clone RMT3-23	BioLegend	Cat#119723; RRID: AB_2616908; Lot#B318424
Brilliant Violet 510™ anti-mouse CD8a Antibody, clone 53-6.7	BioLegend	Cat#100752; RRID: AB_2563057; Lot#B337862
CD223 (LAG-3) Monoclonal Antibody (eBioC9B7W (C9B7W)), PE-Cyanine7	Thermo Fisher Scientific	Cat#25-2231-82; RRID: AB_2573428; Lot#4284448
PerCP/Cyanine5.5 anti-mouse CD3 Antibody, clone 17A2	BioLegend	Cat#100218; RRID: AB_1595492; Lot#B326440
APC anti-mouse CD62L Antibody, clone MEL-14	BioLegend	Cat#104412; RRID: AB_313099; Lot#B223862
CD152 (CTLA-4) Monoclonal Antibody (UC10-4B9), PE	Thermo Fisher Scientific	Cat#12-1522-82; RRID: AB_465879; Lot#4275294
Brilliant Violet 510™ anti-mouse CD8a Antibody, clone 53-6.7	BioLegend	Cat#100751; RRID: AB_2561389; Lot#B323243
CD45 Monoclonal Antibody (30-F11), PE-Cyanine7	Thermo Fisher Scientific	Cat#25-0451-81; RRID: AB_2716950; Lot#2123773
CD3 Monoclonal Antibody (17A2), eFluor™ 450	Thermo Fisher Scientific	Cat#48-0032-82; RRID: AB_1272193; Lot#4314440
PerCP/Cyanine5.5 anti-mouse CD62L Antibody, clone MEL-14	BioLegend	Cat#104432; RRID: AB_2285839; Lot#B209165
FITC anti-mouse CD19 Antibody, clone 6D5	BioLegend	Cat#115506; RRID: AB_313641; Lot#B158637
Ly-6G/Ly-6C Monoclonal Antibody (RB6-8C5), eFluor™ 450	Thermo Fisher Scientific	Cat#48-5931-80; RRID: AB_1548797; Lot#2241983
CD45 Monoclonal Antibody (30-F11), PE-Cyanine7	Thermo Fisher Scientific	Cat#25-0451-81; RRID: AB_2716950; Lot#2123773
APC anti-mouse NK-1.1 Antibody, clone PK136	BioLegend	Cat#108710; RRID: AB_313397; Lot#B229690
PerCP anti-mouse/human CD11b Antibody, clone M1/70	BioLegend	Cat#101230; RRID: AB_2129374; Lot# B256661
BD Horizon™ BUV395 Rat Anti-Mouse CD45, clone 30-F11	BD Biosciences	Cat#565967; RRID: AB_2739420; Lot#2259607, Lot#2259807
BD Horizon™ BUV496 Rat Anti-Mouse CD4, clone GK1.5	BD Biosciences	Cat#612952; RRID: AB_2813886; Lot#3962211, Lot#1328397
BD OptiBuild™ BUV563 Mouse Anti-Mouse NK-1.1, clone PK136	BD Biosciences	Cat#741233; RRID: AB_2870785; Lot#3272326, Lot#3093979

(Continued on next page)

Continued

REAGENT or RESOURCE	SOURCE	IDENTIFIER
BD OptiBuild™ BUV661 Rat Anti-Mouse I-A/I-E, clone M5/114.15.2	BD Biosciences	Cat#750280; RRID: AB_2874471; Lot#3076383
BD Horizon™ BUV805 Rat Anti-Mouse CD8a, clone 53-6.7	BD Biosciences	Cat#612898; RRID: AB_2870186; Lot#3067906
Brilliant Violet 421™ anti-mouse CD54 Antibody, clone YN1/1.7.4	BioLegend	Cat#116141; RRID: AB_2876428; Lot#B376584
Brilliant Violet 510™ anti-mouse CD19 Antibody, clone 6D5	BioLegend	Cat#115545; RRID: AB_2562137; Lot#; Lot#B380219
Brilliant Violet 570™ anti-mouse CD11c Antibody, clone N418	BioLegend	Cat#117331; RRID: AB_10900261; Lot#B369277
Brilliant Violet 605™ anti-mouse CD279 (PD-1) Antibody, clone 29F.1A12	BioLegend	Cat#135219; RRID: AB_2562616; Lot#B333823
BD OptiBuild™ BV711 Rat Anti-Mouse CD106, clone 429	BD Biosciences	Cat#740675; RRID: AB_2740362; Lot#3076314, Lot# 3251889
PE/Cyanine5 anti-mouse/human CD11b Antibody, clone M1/70	BioLegend	Cat#101210; RRID: AB_312793; Lot#B350747
PerCP/Cyanine5.5 anti-mouse CD11a/CD18 (LFA-1) Antibody, clone H155-78	BioLegend	Cat#141007; RRID: AB_10694862; Lot#B378808, Lot#B398985
PE/Cyanine7 anti-mouse CD13 Recombinant Antibody, clone QA19A79	BioLegend	Cat#164008; RRID: AB_2927915; Lot#B375337
APC anti-mouse CD31 Antibody, clone 390	BioLegend	Cat#102409; RRID: AB_312904; Lot#B365398
Ly-6G/Ly-6C Monoclonal Antibody (RB6-8C5), Alexa Fluor™ 700	Thermo Fisher Scientific	Cat#56-5931-82; RRID: AB_494007; Lot#2460072, Lot#E09029-1631
Brilliant Violet 421™ Rat IgG2b, κ Isotype Ctrl Antibody	BioLegend	Cat#400639; RRID: AB_10895758; Lot#B376143
Brilliant Violet 605™ Rat IgG2a, κ Isotype Ctrl Antibody	BioLegend	Cat#400539; RRID: AB_11126979; Lot#B360652
BD Horizon™ BV711 Rat IgG2a, κ Isotype Control	BD Biosciences	Cat#563047; RRID: AB_2869451; Lot#3090569
PerCP/Cyanine5.5 Rat IgG1, κ Isotype Ctrl Antibody	BioLegend	Cat#400425; RRID: AB_893689; Lot#B361880
APC Rat IgG2a, κ Isotype Ctrl Antibody	BioLegend	Cat#400511; RRID: AB_2814702; Lot#B382872
Rat anti-Mouse CD54 (ICAM-1) Monoclonal Antibody (YN1/1.7.4), FITC	Thermo Fisher Scientific	Cat#11-0541-82; RRID: AB_465094; Lot#2083928, Lot#2238585
Rat IgG2b kappa Isotype Control (eB149/10H5), FITC	Thermo Fisher Scientific	Cat#11-4031-82; RRID: AB_470004; Lot#1995330, Lot#2122634
InVivoMAb anti-mouse PD-1 (CD279), clone RMP1-14	BioX Cell	Cat#BE0146; RRID:AB_10949053; Lot#665417S1, Lot#695318A1
InVivoMAb anti-mouse CTLA-4 (CD152), clone 9D9	BioX Cell	Cat#BE0164; RRID:AB_10949609; Lot#63617J2
InVivoMAb rat IgG2a isotype control, clone 2A3	BioX Cell	Cat#BE0089; RRID:AB_1107769; Lot#686318F1
InVivoMAb mouse IgG2b isotype control, clone MPC-11	BioX Cell	Cat#BE0086; RRID:AB_1107791; Lot#645417J3
Rat anti-Mouse CD54 (ICAM-1) Monoclonal Antibody (YN1/1.7.4), Functional Grade	Thermo Fisher Scientific	Cat#16-0541-85; RRID: AB_468980; Lot#2362876, Lot#2452206

(Continued on next page)

Continued

REAGENT or RESOURCE	SOURCE	IDENTIFIER
Rat IgG2b kappa isotype; clone eB149/10H5	Thermo Fisher Scientific	Cat#16-4031-85; RRID: AB_470152; Lot#2345592
Goat anti-Human/Mouse/Rat CD31/PECAM-1 Antibody	R and D Systems	Cat# AF3628; RRID: AB_2161028; Lot# YZU0119021
Goat anti-Mouse Aminopeptidase N/CD13 Antibody	R and D Systems	Cat#AF2335; RRID: AB_2227288; Lot#VRR0322032
Rat anti-Mouse CD54 (ICAM-1) Monoclonal Antibody (YN1/1.7.4)	Thermo Fisher Scientific	Cat#14054182; RRID: AB_467301; Lot#2177738
Donkey anti-Goat IgG (H+L) Cross-Adsorbed Secondary Antibody, Alexa Fluor™ 488	Thermo Fisher Scientific	Cat#A11055; RRID: AB_2534102; Lot#2211210
Donkey anti-Rat IgG (H+L) Cross-Adsorbed Secondary Antibody, DyLight™ 650	Thermo Fisher Scientific	Cat# SA5-10029; RRID:AB_2556609; Lot#VH3056141
FLEX Polyclonal Rabbit Anti-Human CD3	Agilent Dako	Cat#GA50361-2; RRID:AB_2732001
Melan-A, Clone A103, FLEX RTU Monoclonal Mouse Anti-Human	Agilent Dako	Cat# IR63361-2; RRID:AB_2335691
Melanosome, Clone HMB-45, FLEX RTU Monoclonal Mouse Anti-Human	Agilent Dako	Cat#GA05261-2; RRID:AB_2335682
CONFIRM anti-CD34 (QBEnd/10) Primary Antibody Mouse Anti-Human	Roche	Cat# 790-2927; RRID:AB_2336013
CD54/ICAM-1 (E3Q9N) XP® Rabbit mAb	Cell Signaling Technology	Cat#67836; RRID:AB_2799738
GFAP (E4L7M) XP® Rabbit mAb	Cell Signaling Technology	Cat#80788; RRID:AB_2799963
CD16/CD32 Monoclonal Antibody (93)	Thermo Fisher Scientific	Cat# 14-0161-85; RRID:AB_467134
anti-gp100	Abcam	Cat#ab137078; RRID:AB_2732921; Lot# GR304976-9
anti-rabbit IgG horse radish peroxidase (HRP) antibody	Novus Biologicals	Cat# NB7160; RRID: AB_10124655; Lot# P39
mouse anti-β-actin IgG1 antibody	Santa Cruz Biotechnology	Cat# sc-47778; RRID:AB_2714189; Lot#
anti-mouse IgG1 HRP	Bethyl Laboratories	Cat#A90-205P; RRID:AB_10634122; Lot# A90-205P-3
Biological samples		
Preclinical mouse models of brain metastases	This paper	N/A
Brain metastasis patient samples	This paper	N/A
Chemicals, peptides, and recombinant proteins		
Matrigel® Growth Factor Reduced (GFR) Basement Membrane Matrix	Corning	Cat#356231
Isofluran CP 1 ml/ml	CP-Pharma	Cat#1214
Ketabel (Ketamin 100 mg/ml)	Bela-Pharm	Cat#402581.00.00
Rompun 2% (Xylazine)	Elanco	PZN: 01320422
hgp100(25-33) peptide	GenScript	Cat#RP20344
SIINFEKL peptide, Ovalbumin (257-264) chicken	Sigma-Aldrich	Cat#S7951
Recombinant human IL-2 (Proleukin S)	Novartis Pharma	PZN: 02238131
Tetramethylrhodamine Isothiocyanate-dextran (average mol wt 500,000)	Sigma-Aldrich	Cat#52194-1G
10X Spectral DAPI	Akoya Biosciences	Cat#SKU FP1490

(Continued on next page)

Continued

REAGENT or RESOURCE	SOURCE	IDENTIFIER
4',6-Diamidino-2-phenyl-indol-dihydrochlorid (DAPI)	Sigma-Aldrich	Cat# D8417
Critical commercial assays		
Fixable viability Dye, eFluor780	Thermo Fisher Scientific	Cat#65-0865-18
LIVE/DEAD fixable Near IR (780) Viability Kit	Thermo Fisher Scientific	Cat#L34994
CD8a+ T Cell Isolation Kit, mouse	MACS Miltenyi Biotec	Cat#130-095-236
CellTracker™ Green CMFDA Dye	Thermo Fisher Scientific	Cat#C2925
Cytofix/Cytoperm Fixation /Permeabilization Solution Kit	BD Biosciences	Cat#554714
OneComp eBeads	Thermo Fisher Scientific	Cat#01-1111-42
ArC Amin-reactive Compensation Bead kit	Thermo Fisher Scientific	Cat#A10346
Deposited Data		
Single-cell RNA sequencing of human brain metastases	Gonzalez et al. ²³	GEO: GSE186344
Experimental models: Cell lines		
Mouse: Ret (cutaneous melanoma, female origin)	Laboratory of Victor Umansky	N/A
Mouse: Ret CM (cutaneous melanoma, female origin)	Laboratory of Iris Helfrich	N/A
Mouse: Ret CM TyrKO (cutaneous melanoma, Tyr ^{-/-} , female origin)	Laboratory of Iris Helfrich, Laboratory of Michael Hözel	N/A
Mouse: HCmel12 (cutaneous melanoma, male origin)	Laboratory of Thomas Tütting, Bald et al. ⁵²	N/A
Mouse: GL261 (glioma, de-sexualized)	Laboratory of Michael Platten	DSMZ Cat# ACC-802, RRID:CVCL_Y003
Mouse: E0771 (mammary carcinoma, female origin)	Laboratory of Cyrus M. Ghajar	CRL-3461, RRID:CVCL_GR23
Experimental models: Organisms/strains		
Mouse: C57BL/6J	Janvier Labs	RRID:IMSR_RJ:C57BL-6JRJ
Mouse: B6.Cg-Thy1a/Cy Tg(TcrαTcrβ)8Rest/J	Overwijk et al. ⁵³	RRID:IMSR_JAX:005023
Mouse: C57BL/6-Tg(TcrαTcrβ)1100Mjb/J	Hogquist et al. ⁵⁴	RRID:IMSR_JAX:003831
Mouse: B6.Cg-Tg(Lck-cre)548Jxm	Hennet et al. ⁵⁵	RRID:IMSR_JAX:003802
Mouse: B6.Cg-Gt(ROSA)26Sor ^{tm1(CAG-tdTomato)Hze}	Madisen et al. ⁵⁶	RRID:IMSR_JAX:007914
Mouse: B6.Cg-Gt(ROSA)26Sor ^{tm1(CAG-tdTomato)Hze} Tg(Lck-cre)548Jxm	This paper	N/A
Software and algorithms		
FlowJo v10.9.0	BD Biosciences	https://www.flowjo.com ; RRID:SCR_008520
Imaris v7.5.2	Bitplane / Oxford Instruments	https://imaris.oxinst.com/products/imaris-essentials
Ilastik v1.3.3post3	Berg et al. ⁵⁷	https://www.ilastik.org ; RRID:SCR_015246
Arivis Vision 4D v3.3	Arivis AG/ Carl Zeiss Microscopy	https://www.arivis.com/arivis-news/arivisvision4d40 ; RRID:SCR_018000
Fiji (Image J 1.53c)	Schindelin et al. ⁵⁸	https://imagej.net/software/fiji ; RRID:SCR_00228
Graph Pad Prism v9.1.2	GraphPad Software	https://www.graphpad.com ; RRID:SCR_002798
ZenBlack Version 2.3	Carl Zeiss Microscopy	https://www.micro-shop.zeiss.com/de/de/softwarefinder/software-categories/zen-black/ ; RRID:SCR_018163
ZenBlue Version 3.5	Carl Zeiss Microscopy	https://www.micro-shop.zeiss.com/de/de/softwarefinder/software-categories/zen-blue/ ; RRID:SCR_013672

(Continued on next page)

Continued

REAGENT or RESOURCE	SOURCE	IDENTIFIER
Adobe Illustrator v27.6.1	Adobe	https://www.adobe.com/de/products/illustrator.html ; RRID:SCR_010279
Adobe Premiere Pro v15.41	Adobe	https://www.adobe.com/de/products/premiere.html ; RRID:SCR_021315
Inkscape 1.0.2-2	Inkscape	https://inkscape.org/ ; RRID:SCR_014479
R	https://www.r-project.org/	https://www.r-project.org/ ; RRID:SCR_001905
Seurat	https://satijalab.org/seurat/	https://satijalab.org/seurat/ ; RRID:SCR_016341
Phenochart™ v1.1.0	Akoya Biosciences	https://www.akoyabio.com/support/software/
inForm v2.6.0	Akoya Biosciences	https://www.akoyabio.com/phenoimager/inform-tissue-finder/

EXPERIMENTAL MODEL AND STUDY PARTICIPANT DETAILS

Animals and surgical procedures

For adoptive T cell transfer (ACT) male C57BL/6J mice (>8 weeks of age, >20g body weight, Janvier Labs) were used as acceptor mice. Homozygous pmel-1 mice (B6.Cg-Thy1^a/Cy Tg(TcraTcrb)8Rest/J (RRID:IMSR_JAX:005023),⁵³ male, >6 weeks of age, inhouse bred, and homozygous OT-I mice (C57BL/6-Tg(TcraTcrb)1100Mjb/J)⁵⁴ (kind gifts from Prof. Michael Platten, Heidelberg, Germany) were used as T cell donors.

To visualize endogenous T cells, a transgenic mouse line in which Cre recombinase was expressed under a lymphocyte protein tyrosine kinase (LCK) promotor B6.Cg-Tg(Lck-cre)548Jxm (RRID:IMSR_JAX:003802)⁵⁵ (a kind gift from Prof. Ana Martin-Villalba) was crossed with a transgenic mouse that expressed floxed tdTomato (tdTom) B6.Cg-Gt(ROSA)26Sor^{tm14(CAG-tdTomato)Hze} mice (RRID:IMSR_JAX:007914)⁵⁶ (a kind gift from Dr. Darjus Tschaharganeh). This resulted in the T cell reporter mouse line (B6.Cg-Gt(ROSA)26Sor^{tm14(CAG-tdTomato)Hze} Tg(Lck-cre)548Jxm) LCK-Cre^{+/−} x lox-stop-lox (LSL)-tdTomato^{+/+} or ^{+/-}, here referred to as LCK-Cre x LSL-tdTomato.

Animals were housed under specific pathogen-free conditions at the DKFZ animal care facility. All animal procedures were approved by the Regierungspraesidium Karlsruhe, Germany (local governmental authority for laboratory animal research).

Chronic cranial window implantation

LCK-Cre x LSL-tdTomato mice (>8 weeks of age, >20g body weight) and C57BL/6J acceptor mice underwent surgical procedure to implant a chronic cranial window (6 mm diameter) and a titan ring for painless head fixation during IVM as described before.⁵⁹ To ensure equal experimental settings without inflammation, mice were allowed to recover for at least 3 weeks following cranial window surgery until flank tumor inoculation and cortical tumor injections were performed.

Flank tumor inoculation

For flank tumor inoculation, mice were anesthetized using isoflurane (maximum 5% in 0.5 l/min O₂ for initiation, followed by maximum 2% in 0.5 l/min O₂) and the flank was shaved and disinfected. A volume of 100 µl comprising 150,000 murine melanoma cells in a 1:1 mixture with Matrigel (Corning) was injected subcutaneously (s.c.).

Cortical and striatal tumor injection

For cortical tumor injection (TI) two days post s.c. flank tumor injection, mice were anaesthetized with a Ketamin/Xylazin mix (Ketamin 100 mg/kg, Xylazin 10 mg/kg, intraperitoneal injection) and the window cover glass was carefully removed. Fluorescently labeled murine melanoma cells resuspended in PBS were centrifuged at 500 rcf, PBS supernatant was removed and pelleted cells were directly loaded into a 10 µl Hamilton syringe (Hamilton, WICOM Heppenheim, Hamilton Bonaduz 701 10µL, Ref.: 80300). 0.1-0.2 µl of pelleted cells were stereotactically injected into the mouse cortex using a motorized Stoelting QSI Quintessential Stereotaxic Injector (Stoelting No 53311) at an injection speed of 0.1 µl/min at a depth of approximately 500 µm with an angle of 45° into the parietal lobe, resulting in 30,000-100,000 cortically injected cells. The tumor injection site was in the center of the hemisphere accessible through the window approx. 1 - 1.5 mm lateral of the sagittal sinus and approx. 0.5 - 1 mm distal from large cortical vessels, as rupture of these vessels during the injection procedure could lead to fatal bleeding. The window was resealed with a new 6 mm cover glass. Injections into the striatum were performed in mice without cranial windows. The skull was exposed by creating a small incision in the skin along midline of the skull. Using a surgical drill, a small hole was created in the mouse skull and subsequently 30,000-100,000 fluorescent tumor cells were injected as described above, however at a depth of 3 mm to reach the striatum. Following injection, the skin is sutured.

Adoptive T cell transfer

To follow *ex vivo* labeled fluorescent T cells that specifically recognize the melanoma antigen gp100, adoptive T cell transfer of *ex vivo* stimulated CD8+ pmel-1 T cells was performed.⁶⁰ For ACT with antigen-unspecific T cells, CD8+ OT-I T cells were isolated from OT-I transgenic mice. On day 5 post cortical flank tumor injection, lymphocytes were isolated from spleen and inguinal, axial, mesenteric and cervical lymph nodes of naïve pmel-1 or OT-I donor mice. The organs were mashed through a 70 µm cell strainer to generate a single cell suspension, erythrocytes were lysed by incubating in ACK lysis buffer (Gibco, # A104920) on ice for 90 sec. The cells were cultured *in vitro* for three days at 37 °C, 5% CO₂ in RPMI1640 (PAN-Biotec #P04-18500) supplemented with 10% FBS (Gibco, #10500-064, Lot 08Q5107K), 100 U ml⁻¹ penicillin, 100 µg ml⁻¹ streptomycin (Sigma-Aldrich), 50 µM 2-mercaptoethanol (Gibco), 2 mM L-glutamine (Gibco), 25mM HEPES buffer (Gibco), 1 mM sodium pyruvate (Gibco), 0.1M non-essential amino-acid (Gibco), 2 µg/ml hgp100₂₅₋₃₃ peptide (GenScript, #RP20344) or 2 µg/ml SIINFEKL peptide (Ovalbumin₂₅₇₋₂₆₄, Sigma-Aldrich, #S7951) for pmel-1 or OT-I T cells respectively, and 30 U/ml IL-2 (Proleukin, Novartis) for *in vitro* stimulation. On day 8 post cortical tumor inoculation, *in vitro* activated lymphocytes were harvested and CD8+ T cells were enriched by using a “CD8a+ T Cell Isolation Kit, mouse” (MACS Miltenyi Biotec, # 130-095-236) according to manufacturer’s instructions, fluorescently labeled with 1 µM-2.5 µM CellTracker™ Green CMFDA Dye (Thermo Fisher Scientific, #C2925), and subsequent ACT was performed by intravenous injection of 5 × 10⁶ T cells in 100 µl PBS in the lateral tail vein of tumor bearing acceptor mice.

In vivo two-photon laser scanning microscopy (IVM)

For IVM mice were anesthetized using isoflurane (maximum 5% in 0.5 l/min O₂ for initiation) for painless fixation in a custom-made holder. Then anesthesia was continued through a nose mask with maximum 2% isoflurane in 0.5 l/min O₂ for imaging using a Zeiss LSM 7 MP equipped with a Chameleon Ultra II laser or a Discovery NX laser (both from Coherent), a 20x/1.0 W-Plan-Apochromat objective (Carl Zeiss Microscopy) and using BP500-550nm / BP575-610nm optical filters (Carl Zeiss Microscopy). To visualize vasculature *in vivo*, i.v. injection of 100 µL of tetramethylrhodamine-isothiocyanate-Dextran (5 mg mL, TRITC Dextran; average MW: 500,000, Sigma-Aldrich, USA) into the lateral tail vein was performed directly prior to imaging. TRITC injection was omitted when anti-ICAM-1 FITC was injected. For visualization of GFP, CMFDA and tdTomato an excitation wavelength of 950 nm was used, for ICAM-1-FITC 750 nm and for TRITC-Dextran 850 nm was used. Lowest adequate laser power and a gains ranging from 600 to 800 was used for image acquisition. Z steps were 3-10 µm depending on the experiment (10 µm for volume measurements and timeseries, 3 – 5 µm for stacks of specific regions).

ACT model mice were analyzed regularly between day 5 and day 14 post cortical tumor injection by IVM, LCK-Cre x LSL-tdTomato mice were analyzed regularly between day 1 and day 14 post cortical tumor injection.

Immune-checkpoint therapy

For immune checkpoint therapy, animals were treated by intraperitoneal injection with 250 µg anti-PD-1 (BioX Cell #BE0146, RRID:AB_10949053, Lot 665417S1, Lot 695318A1) and 100 µg anti-CTLA-4 (BioX Cell #BE0164, RRID:AB_10949609, Lot 63617J2), or isotype antibodies (BioX Cell #BE0089, RRID:AB_1107769, Lot 686318F1; BioX Cell #BE0086, RRID:AB_1107791, Lot 645417J3) for the ICI and control group respectively, starting from day 7 post cortical injection every two days until the end of the experiment.

Monitoring of flank tumor size

Using caliper measurement every 2-4 days post s.c. flank tumor injection, the long tumor diameter *D* and the short tumor diameter *d* were measured respectively, and the tumor volume was calculated as: Volume = (*D* × *d*²) / 2.

Cell lines

The murine melanoma cell lines Ret (a kind gift from V. Umansky, Mannheim, Germany), Ret CM TyrKO, HCmel12⁵² (a kind gift from J. Landsberg and T. Tüting, Bonn, Germany, genetically modified by D. Hinze to generate HCmel12^{Tyr-/-} (HCmel12 TyrKO) cells) and HCmel12 TyrKO were cultured in RPMI 1640 medium with 10% fetal bovine serum (FBS) (Gibco, #105000-064, Lot 08Q5107K), 100 U ml⁻¹ penicillin, 100 µg ml⁻¹ streptomycin (Sigma-Aldrich), and 1% L-Glutamine at 37°C and 5% CO₂. To avoid interference of pigmented cells with fluorescence microscopy, Tyrosinase was stably knocked out in Ret CM and HCmel12 cells using CRISPR-Cas9 technology. For Ret CM TyrKO cells, four brain passages were performed to increase brain tropism.⁶¹ For IVM experiments, Tyrosinase KO (TyrKO) cells were transduced with expression vectors for red fluorescent protein (tdTomato) or green fluorescent protein (GFP).

GL261 gp100-over-expressing cells (a kind gift from Prof. Michael Platten) and the murine tdTomato-expressing brain-passaged mammary adenocarcinoma E0771 cell line (a kind gift from Cyrus M. Ghajar) were cultured in Dulbecco's modified Eagle's medium (DMEM) supplemented with 10 % (FBS), 100 U ml⁻¹ penicillin, and 100 µg ml⁻¹ streptomycin (Sigma-Aldrich) at 37 °C, 5% CO₂. All cells were regularly tested in-house for mycoplasma contamination by PCR.

Brain metastasis patient samples

The utilization of FFPE tumor material for the immunohistochemical analyses was approved by the ethics committee of the University of Dresden (EK 48022018). The studies were conducted in accordance with the Declaration of Helsinki.

METHOD DETAILS

Immuno-blotting

For melanoma antigen gp100 expression analysis, cell pellets were lysed with protein lysis buffer and diluted with Lämmli-Buffer 1:4. Protein concentration was determined by Bradford assay and a total of 50 µg of protein was loaded per well on a 10% SDS-acrylamide gel. Gel electrophoreses was performed at 120 V in running buffer. Protein was transferred from the gel to a nitrocellulose membrane by semi-dry blotting. The membrane was blocked with 5% powdered milk for 45 min at room temperature (RT), subsequently membrane was incubated with anti-gp100 antibody (Abcam, ab137078, RRID:AB_2732921, Lot GR304976-9) (diluted 1:1000 in 5% milk) at 4°C over night. After washing three times with TBS-T, the membrane was incubated with secondary anti-rabbit IgG horse radish peroxidase (HRP) antibody (Novus Biologicals, NB7160, RRID:AB_10124655, Lot P39) (diluted 1:5000 in 5% milk) for 45 min at RT. HRP signal was developed with ECL Substrate and images were taken by ChemiDoc MP imaging system (BioRad). After stripping with stripping buffer (62.5 mM TRIS HCl pH 6.8, 2% SDS, 0.7% beta-mercaptoethanol) at 50°C for 30 min, the membrane was incubated with mouse anti-β-actin IgG1 antibody (Santa Cruz Biotechnology, # sc-47778, RRID:AB_2714189) (diluted 1:1000 in 5% milk) overnight at 4°C and subsequently with secondary antibody anti-mouse IgG1 HRP (Bethyl Laboratories, #A90-205P, RRID:AB_10634122, Lot A90-205P-3) (diluted 1:5000 in 5% milk) for 45 min at RT and images were taken with ChemiDoc MP (Bio-Rad Laboratories) imaging system.

Flow Cytometry

For flow cytometric analysis of pmel-1 T cells, lymphocytes were isolated from lymph nodes (inguinal, axial, cervical, mesenteric) and spleen of pmel-1 homozygous mice. The organs were meshed through a 70 µm cell strainer for producing a single cell suspension, erythrocytes of spleen samples were lysed by incubating in ACK lysing buffer (Gibco, # A104920) on ice for 90 seconds. The cells were cultured *in vitro* for three days as described above (see Adoptive T cell transfer section). *In vitro* activated lymphocytes and lymphocytes freshly isolated from a pmel-1 mouse (unstimulated control) were harvested and CD8⁺ T cells were enriched by using a “CD8a+ T Cell Isolation Kit, mouse” (Milteny, # 130-095-236). Cells were washed with PBS and blocked with anti-CD16/anti-CD32 (eBiosciences, 14-0161-85, RRID:AB_467134) for 20 min on ice and were incubated with antibody panels 1 and 2 (see table below, surface marker staining) for 45 min on ice.

For flow cytometric analysis of tdTomato expression in lymphocytes isolated from LCK-Cre x LSL-tdTomato mice, lymphocytes were isolated from lymph nodes (inguinal, axial, cervical, mesenteric) and spleen of two LCK-Cre^{-/-} x LSL-tdTomato^{+/+} mice as negative controls, as described above. After erythrocyte lysis, lymphocytes were washed with PBS and blocking and flow cytometry staining with surface marker panel 3 (see table below) were performed as described above.

For compensation, single color stainings were measured using OneComp eBeads (Invitrogen, #01-1111-42) and ArC Amin-reactive Compensation Bead kit (Invitrogen, A10346). Cells were analyzed on a BD FACS Canto II equipped with UV (405 nm), blue (488 nm) and red (633 nm) laser and subsequent data analysis was performed using FlowJo software v10.9.0.

For spectral flow cytometric analysis of immune cells, endothelial cells and pericytes isolated from the brain of LCK-Cre x LSL-tdTomato mice with HCmel12 TyrKO GFP brain tumors, mice were sacrificed on day 10 post cortical tumor injection by cardiac perfusion with PBS. The brain was isolated, the two hemispheres were separated and a region of approx. 4 x 4 mm around the tumor injection site was isolated from the cortex, and a region of equivalent size and location was isolated from the contralateral non-tumor bearing hemisphere. To enrich immune cells from each hemisphere, the hemispheres were cut into small pieces and each sample was digested in 3 mL 50 µg/mL Liberase TL (Roche) for 30 min at 37°C. Subsequently the brain tissue was meshed first through a 100 µm cell strainer, then through a 70 µm cell strainer and cell strainers were washed with Hank's balanced salt solution (HBSS). After washing with HBSS, the digested brain tissue was centrifuged for 30 min at 1467 x g on a 25% Percoll continuous gradient without active deceleration. After centrifugation, the myelin layer on top was removed carefully. The rest of the sample was topped up to 50 mL with PBS and centrifuged at 500 x g for 10 min. After enrichment of immune cells and myelin removal, the cells were blocked with human anti-CD16/ anti-CD32 for 15 min on ice, then surface marker staining with the antibodies of panel 4 was performed for 30 min on ice. Cells were washed with PBS, fixed using BD Cytofix/Cytoperm and were kept on ice until data was acquired using an ID7000™ Spectral Cell Analyzer (Sony Biotechnology) equipped with 5 lasers. FlowJo Version v10.9.0 (was used for data analysis, gates were set according to the appropriate fluorescence minus one (FMO) controls).

	Clone	Company	Reference number	Lot#	RRID
Antibodies – Panel 1					
Fixable viability Dye, eFluor780		eBioscience	65-0865-18		
CD279(PD-1), PE	J43	eBioscience	12-9985-83	E0231-1634	AB_466296
CD3, PE/Cyanine7	17A2	BioLegend	100220	B185661	AB_1732057
CD8a, PerCP-Cyanine5.5	53-6.7	eBioscience	45-0081-82	2151510	AB_1107004
CD4, Pacific Blue	RM4-5	BioLegend	100531	B255834	AB_493374
CD44, Brilliant Violet 510	IM7	BioLegend	103043	B227210	AB_2650923

(Continued on next page)

Continued

	Clone	Company	Reference number	Lot#	RRID
CD69, APC	H1.2F3	eBioscience	17-0691-82	2065643	AB_1210795
Antibodies – Panel 2					
Fixable viability Dye, eFluor780		eBioscience	65-0865-18		
CD4, FITC	GK1.5	eBioscience	11-0041-85	1987705	AB_464893
CD366 (Tim-3), Brilliant Violet 421	RMT3-23	BioLegend	119723	B318424	AB_2616908
CD8a, Brilliant Violet 510	53-6.7	BioLegend	100752	B337862	AB_2563057
CD223 (LAG-3), PE-Cyanine7	C9B7W	eBioscience	25-2231-82	4284448	AB_2573428
CD3e, PerCP-Cyanine5.5	17A1	BioLegend	100218	B326440	AB_1595492
CD62L, APC	MEL-14	BioLegend	104412	B223862	AB_313099
CD152 (CTLA-4), PE	UC10-4B9	eBioscience	12-1522-82	4275294	AB_465879
Antibodies – Panel 3					
Fixable viability Dye, eFluor780		eBioscience	65-0865-18		
CD4, FITC	GK1.5	eBioscience	11-0041-85	1987705	AB_464893
CD8a, Brilliant Violet 510	53-6.7	BioLegend	100751	B323243	AB_2561389
CD45, PE-Cyanine7	30-F11	eBioscience	25-0451-81	2123773	AB_2716950
CD3e, eFluor 450	17A2	eBioscience	48-0032-82	4314440	AB_1272193
CD62L, PerCP/Cyanine5.5	MEL-14	BioLegend	104432	B209165	AB_2285839
CD69, APC	H1.2F3	eBioscience	17-0691-82	2065643	AB_1210795
CD19, FITC	6D5	BioLegend	115506	B158637	AB_313641
Ly-6G/Ly-6C, eFluor450	RB6-8C5	eBioscience	48-5931-80	2241983	AB_1548797
CD45, PE-Cyanine7	30-F11	eBioscience	25-0451-81	2123773	AB_2716950
NK-1.1, APC	PK136	BioLegend	108710	B229690	AB_313397
CD11b, PerCP	M1/70	BioLegend	101230	B256661	AB_2129374
Antibodies – Panel 4					
LIVE/DEAD fixable Near IR (780) Viability Kit		Invitrogen	L34994		
BUV395 Rat Anti-Mouse CD45	30-F11	BD Biosciences	565967	2259607, 2259807	AB_2739420
BUV496 Rat Anti-Mouse CD4	GK1.5	BD Biosciences	612952	3962211, 1328397	AB_2813886
BUV563 Mouse Anti-Mouse NK-1.1	PK136	BD Biosciences	741233	3272326, 3093979	AB_2870785
BUV661 Rat Anti-Mouse I-A/I-E	M5/114.15.2	BD Biosciences	750280	3076383	AB_2874471
BUV805 Rat Anti-Mouse CD8a	53-6.7	BD Biosciences	612898	3067906	AB_2870186
Brilliant Violet 421™ anti-mouse CD54	YN1/1.7.4	Biolegend	116141	B376584	AB_2876428
Brilliant Violet 510™ anti-mouse CD19	6D5	Biolegend	115545	B380219	AB_2562137
Brilliant Violet 570™ anti-mouse CD11c	N418	Biolegend	117331	B369277	AB_10900261
Brilliant Violet 605™ anti-mouse CD279 (PD-1)	29F.1A12	Biolegend	135219	B33823	AB_2562616
Rat Anti-Mouse CD106	429	BD Biosciences	740675	3076314	AB_2740362
PE/Cyanine5 anti-mouse/human CD11b	M1/70	Biolegend	101210	B350747	AB_312793
PerCP/Cyanine5.5 anti-mouse CD11a/CD18 (LFA-1)	H155-78	Biolegend	141007	B378808, B398985	AB_10694862
PE/Cyanine7 anti-mouse CD13	QA19A79	Biolegend	164008	B375337	AB_2927915
APC anti-mouse CD31	390	Biolegend	102409	B365398	AB_312904
Ly-6G/Ly-6C Monoclonal Antibody (RB6-8C5), Alexa Fluor™ 700	RB6-8C5	eBioscience	56-5931-82	2460072, E09029-1631	AB_494007
Brilliant Violet 421™ Rat IgG2b, κ Isotype Ctrl Antibody	RTK4530	Biolegend	400639	B376143	AB_10895758
Brilliant Violet 605™ Rat IgG2a, κ Isotype Ctrl Antibody	RTK2785	Biolegend	400539	B360652	AB_11126979
BV711 Rat IgG2a, κ Isotype Control	R35-95	BD Biosciences	563047	3090569	AB_2869451

(Continued on next page)

Continued

	Clone	Company	Reference number	Lot#	RRID
PerCP/Cyanine5.5 Rat IgG1, κ Isotype Ctrl Antibody	RTK2071	Biolegend	400425	B361880	AB_893689
APC Rat IgG2a, κ Isotype Ctrl Antibody	RTK2758	Biolegend	400511	B382872	AB_2814702

In vivo antibody staining

For *in vivo* antibody staining of vascular ICAM-1, 100 µg anti-ICAM-1 FITC (Invitrogen #11-0541-82, RRID:AB_465094, Lots 2083928, 2238585) or respective isotype control antibody (Invitrogen #11-4031-82, RRID:AB_470004, Lots 1995330, 2122634) were injected into the lateral tail vein of LCK-Cre x LSL-tdTomato mice on day 10 post cortical TI. ICAM-1 FITC signal was analyzed by IVM before and 1-3h post i.v. injection of labeled anti-ICAM-1 antibody.

In vivo functional ICAM-1 blocking

For functional blocking of ICAM-1 *in vivo*, HCmel12 TyrKO tumor bearing LCK-Cre x LSL-tdTomato mice with chronic cranial window were injected with 100 µg anti-ICAM-1 (CD54 (ICAM-1) monoclonal antibody, functional grade; clone YN1/1.7.4; eBioscience #16-0541-85; Lots 2362876, 2452206; RRID: AB_468980) or isotype control antibody (Rat IgG2b kappa isotype; clone eB149/10H5; eBioscience #16-4031-85; Lot 2345592; RRID: AB_470152) i.v. per mouse and timepoint. Antibody injections started at day 3 post cortical TI and were continued every three days until the end of the experiment. T cell infiltration and brain tumor growth were followed by IVM.

Immunofluorescence

For immunofluorescence analysis HCmel12 TyrKO tdTomato cells were injected s.c. into the flank of male C57BL/6 mice >8 weeks of age, followed by cortical injection through a drill hole two days later, as described below. On day 8, ACT was performed as described above and mice were sacrificed by intracardiac perfusion with PBS and 4% PFA. The brains were isolated and were incubated with 4% PFA at RT for 4h. After incubation in 30% sucrose in PBS overnight at 4°C, the brains were frozen in TissueTek Freezing medium and 10 µm thick coronal brain sections were cut with a Cryo-microtome Leica CM3050 S. Sections were air dried for 20-30 min at RT and subsequently blocked with 3% BSA in 0.3% Triton X-100 in PBS at RT for 1h. Primary antibodies (Goat anti m/r CD31 (R&D, #AF3628, RRID:AB_2161028, Lot# YZU0119021) 1:200, Goat anti m CD13(R&D, #AF2335, RRID:AB_2227288, Lot#VR0322032) 1:200, Rat anti-ICAM-1 (Invitrogen, #14054182, RRID:AB_467301, Lot# 2177738) 1:25 diluted in blocking solution) were incubated on slides over night at 4°C. Slides were washed three times with 0.3% TritonX-100 in PBS (PBS-T) before secondary antibody incubation diluted 1:400 in blocking solution (AF488 Donkey Anti-Goat (Invitrogen, #A11055, RRID:AB_2534102, Lot#2211210), Dy-Light650 Donkey anti-Rat (Invitrogen, #SA5-10029, RRID:AB_2556609, Lot# VH3056141) for 1h at RT, subsequent washing with PBS-T for 5 min at RT and incubation with 1 µg/ml DAPI in blocking buffer for 5 min at RT. After two more washing steps with PBS-T, a cover slip was mounted with Vectashield mounting medium. The images were acquired using a Zeiss LSM 780 spinning disk microscope and 63x oil-immersion objective (1.4 Oil Plan-Apochromat). Fiji (ImageJ)⁵⁸ was used for image processing by rolling ball background subtraction and maximum intensity projection (MIP) of up to 3 z-planes and brightness and contrast adjustments.

Multiparametric immunofluorescence

Formalin-fixed paraffin-embedded (FFPE) tissue blocks were cut into 3–5 µm sections. Multi-parametric immunofluorescence stainings of human brain metastasis samples were performed on the Ventana Ultra Instrument (Roche, Basel, Switzerland). Tissues were deparaffinized and antigen retrieval was performed in the cell conditioning 1 solution (Roche). Incubation of each primary antibody followed for 32 min at 36°C. Then, the appropriate secondary antibody (OmniMap anti-mouse or anti-rabbit, ready-to-use, all from Ventana Medical Systems) was applied for 12 min. Finally, one of the tyramide signal amplification (TSA) fluorophores (Akoya Biosciences, OPAL520, OPAL540, OPAL570 or OPAL690) was added to the tissue slides for 8 min. Stripping of the primary and secondary antibodies took place by heating the slides at 100°C in the cell conditioning 2 solution (Roche) for 24 min. This sequence of steps (except deparaffinization and antigen retrieval) was repeated for each primary antibody. Finally, all tissue slides were counterstained with spectral DAPI (Akoya Biosciences) and coverslipped with fluoromount medium (SouthernBiotech, Birmingham, Alabama, USA). The primary antibodies used for the multiplex immunofluorescence stainings are summarized in the table below. The utilization of FFPE tumor material for the immunohistochemical analyses was approved by the ethics committee of the University of Dresden (EK 48022018). The studies were conducted in accordance with the Declaration of Helsinki.

Antigen	Clone	Dilution	Source	RRID
CD3	polyclonal	1:200	Dako	AB_2732001
MelanA	A103	1:300	Dako	AB_2335691
HMB-45	HMB45	1:100	Dako	AB_2335682

(Continued on next page)

Continued

Antigen	Clone	Dilution	Source	RRID
CD34	QBEnd/10	ready to use	Roche	AB_2336013
ICAM-1	E3Q9N	1:100	CellSignaling	AB_2799738
GFAP	E4L7M	1:100	CellSignaling	AB_2799963

All stained sections were whole scanned ($\times 100$ magnification) using the Vectra 3 automated quantitative pathology imaging system (Akoya Biosciences). Relevant areas were marked in the phenochart™ software (Akoya Biosciences) and scanned ($\times 200$ magnification) for all patient slides. The analysis of stainings was performed using the inForm software (Akoya Biosciences) and ImageJ/Fiji.

QUANTIFICATION AND STATISTICAL ANALYSIS

Image Processing and Quantification

Image processing was always performed on the whole image. Tile scan images were stitched using ZenBlack (Carl Zeiss Microscopy). For clearance of channel overlap channel subtraction was performed on two-photon microscopy images using ZenBlack (Carl Zeiss Microscopy) or Fiji.⁵⁸ A Gaussian Filter was applied for smoothing using Imaris (Bitplane) or Fiji. Tumor volume was analyzed from three-dimensional two-photon microscopy images by intensity thresholding in Fiji. Pmel-1 T cells were counted manually using Fiji.

For the analysis of ICAM-1 *in vivo* staining, ICAM-1 signal intensities of two-photon images were measured by analyzing peak intensities at the vessel walls using Fiji. To balance out batch differences between mice, ICAM-1 signal intensities at vessel walls of PVVs were normalized to mean ICAM-1 signal intensities at brain surface capillaries of the respective mouse. T cell signal in the perivascular space within 30 μm of distance from the vessel wall was measured as mean intensity of a binary T cell mask generated by thresholding using Fiji.

For microregional tumor volume measurement over time, regions of interest of 0.00401802 mm^3 were chosen and the same regions of interest based on the vasculature were followed over time from day 9 to day 12 post cortical tumor injection and thresholding was used to quantify tumor volume per region, while transferred T cells of day 10 datasets were counted manually.

Semi-automated three-dimensional T cell tracking of two-photon timeseries images of the ACT model was performed using Imaris (Bitplane). We defined transferred T cells with mean velocity $\geq 50 \text{ nm/s}$ and mean displacement $\geq 10 \text{ nm/s}$ as “motile” and T cells with a mean velocity $< 50 \text{ nm/s}$ and mean displacement $< 10 \text{ nm/s}$ as “stationary”, as these cells stayed within distance of approximately one cell length during a typical time series duration of 25 min. To ensure that T cells that travelled further from its track origin but returned to its origin were not defined as stationary, the mean velocity threshold of 50 nm/s was included into this definition.

Videos from IVM timeseries data were made after pre-processing with Fiji, Zen Black (Zeiss) and Imaris (Bitplane) with Adobe Premiere Pro.

For spatio-temporal analysis of the distribution of transferred pmel-1 T cells at distinct vessel types (Figure 2C), regions of interest (ROIs) containing distinct vessel types were selected manually and volumes of each ROI were determined. T cells were counted manually for each ROI and local T cell density was calculated as T cell number of one ROI / volume (mm^3) of the respective ROI.

For spatio-temporal analysis of the distribution of endogenous T cells of LCK-Cre x LSL-tdTomato mice at distinct vessel types in the LCK-Cre x LSL-tdTomato model (Figure 2D), IVM images were preprocessed using machine learning in Ilastik⁵⁷ for pixel classification of vessels and T cells. Segmented images were further analyzed using Arivis Vision 4D (Arivis AG) by 3D modeling of the vasculature structure and image regions were manually cut to only include distinct vessel types (PVVs, intratumoral vessels, peritumoral capillaries and the sagittal sinus). Subsequent distance map calculations were performed for each vessel type and the volume of T cells within 15 μm proximity of the respective blood vessels according to the distance map was measured and to account for differences in vessel numbers and sizes the T cell volume was normalized to the respective vessel surface area for quantification.

IVM images of T cell infiltration and brain tumor volume of mice under functional *in vivo* ICAM-1 blockage were pre-processed as described above, then machine learning based pixel classification of T cells and tumor cells was performed using Ilastik. Pixel probability maps were used to generate binary images using thresholding in Fiji. Distance map calculation in Fiji was used to determine a 200 μm margin around the binarized tumor volume to define the region of interest, in which the T cell volume was determined. Using the 3D Voxel Counter Plugin in Fiji, the volumes of the tumor region of interest and the cumulative T cell volumes were determined. For quantification of T cell infiltration, the cumulative T cell volume was normalized to the volume of the tumor region of interest. If brain tumors had regressed completely, the tumor region of interest of a timepoint when tumor mass was still detectable was used at the estimated location.

For quantification of multiparametric immunofluorescence images of human melanoma brain metastasis patient samples intratumoral and peritumoral areas were defined manually by assessing distribution and morphology of nuclei, expression of MelanA/HMB45 as tumor markers and presence of GFAP expression. For quantification of vessels Ilastik pixel classification and object detection was used to detect and quantify capillary vessels, large vessels and T cells. As segmentation of individual T cells located in T cell clusters of highly infiltrated tissue was not very accurate, the area covered by T cell per area analyzed was used to quantify T cell infiltration.

Graphical illustrations were made using Inkscape, the graphical abstract was created with BioRender.com.

Single cell RNA-sequencing analysis

Single-cell gene expression data²³ of human brain metastases was obtained from the Gene Expression Omnibus with accession number GSE186344. Data was implemented into Seurat⁶² and pre-processed using the standard Seurat workflow. Cells type assignment was performed using the published annotations obtained from GSE186344. All subsequent analyses were performed using the Seurat package.

Statistical Analysis

Statistics were calculated using GraphPad Prism version 9.1.2.

Data are represented as mean \pm standard error of the mean (SEM) if not stated otherwise. N numbers are reported in the figure legends.

For correlation of microregional tumor growth rate with microregional T cell density linear regression analysis was conducted collectively on 5 microregions of 0.004 mm^3 at the tumor edge per mouse of $n=6$ mice per group treated with ICI or isotype control antibodies.